ABSTRACT

Title of Dissertation:	INTEGRATED QUANTUM PHOTONIC CIRCUITS WITH QUANTUM DOTS
	Shahriar Aghaeimeibodi, Doctor of Philosophy, 2020
Dissertation directed by:	Professor Edo Waks Department of Electrical and Computer Engineering

Scalable quantum photonics require efficient single-photon emitters as well as low-loss reconfigurable photonic platforms that connect and manipulate these single photons. Quantum dots are excellent sources of on-demand single photons and can act as stable quantum memories. Therefore, integration of quantum dots with photonic platforms is crucial for many applications in quantum information processing.

In this thesis, we first describe hybrid integration of InAs quantum dots hosted in InP to silicon photonic waveguides. We demonstrate an efficient transition of quantum emission to silicon. Quantum nature of the emission is confirmed through photon correlation measurements. Secondly, we present a micro-disk resonator device based on silicon photonics that enables on-chip filtering and routing of single photons generated by quantum dots. The tunability of silicon photonics decreases at low temperatures due to “carrier freeze-out”. Because of a strong electro-optic effect in lithium niobate, this material is the ideal platform for reconfigurable photonics, even at

cryogenic temperatures. To this end, we demonstrate integration of quantum dots with thin-film lithium niobate photonics promising for active switching and modulating of single photons.

More complex quantum photonic devices require multiple identical single-photon emitters on the chip. However, the transition wavelength of quantum dots varies because of the slightly different shape and size of each dot. To address this hurdle, we propose and characterize a quantum dot device located in an electrostatic field. The resonance wavelength of the quantum dot emission is tuned up to 8 nm, more than one order of magnitude greater than the transition linewidth, opening the possibility of tuning multiple quantum dots in resonance with each other.

Finally, we discuss the application of a single quantum dot strongly coupled to a nanophotonic cavity as an efficient medium for non-linear phenomenon of optical amplification. Presence of a strong pump laser inverses the population of the quantum dot and leads to stimulated emission from the cavity-coupled quantum dot. Using this platform, we observe an optical gain of ~ 16%, significantly increased compared to previous demonstrations of gain in single solid-state quantum emitters without cavities or weakly coupled to cavities. These demonstrations are significant steps toward robust control of single photons using linear and non-linear photonic platforms.

INTEGRATED QUANTUM PHOTONIC CIRCUITS WITH QUANTUM DOTS

by

Shahriar Aghaeimeibodi

Dissertation submitted to the Faculty of the Graduate School of the
University of Maryland, College Park, in partial fulfillment
of the requirements for the degree of
Doctor of Philosophy
2020

Advisory Committee:
Professor Edo Waks, Chair
Professor Thomas Murphy
Professor Kevin Daniels
Professor Cheng Gong
Professor Steven Rolston

Dedication

I dedicate this thesis to my family.

Acknowledgements

Looking back at my years in the PhD program, I have been extremely lucky to work with so many intelligent, passionate, and kind-hearted people. First of all, I would like to express my deepest gratitude to my advisor Professor Edo Waks for his unwavering support and insightful guidance. He taught me how to think about research, solve problems, and have a big picture. I learnt so many valuable lessons from him over the past years which makes me forever indebted to him. Whenever I had issues or doubts, he always had many solutions in mind. His passion for science, inspires me to continue on the path for a career in academia.

I also would like to express my deep appreciation to my committee members, Professors Thomas Murphy, Cheng Gong, Kevin Daniels, and Steven Rolston. I must also thank my collaborators without whom I could not finish any of my projects. I learnt a lot from my discussions with Professor Mohammad Hafezi who also served on my proposal exam committee. Dr. Christopher Richardson and Dr. Richard P. Leavitt provided us with quantum dot wafers which were essential to the research discussed in this thesis. I enjoyed collaborating with Professors Marko Loncar, Dirk Englund, Yuhuang Wang, and Christopher Monroe. I am also grateful to Dr. Jacques Carolan and Dr. Mehdi Jadidi for many fruitful discussions.

I worked very closely with several postdocs in the group. Special thanks to Professor Jehyung Kim who was a postdoc in the group and a mentor for me from whom I learnt how to make devices, run optics experiments, and many other things. I also had great pleasure of working with Dr. Youngmin Kim, Dr. Changmin Lee, Dr. Hamidreza Chalabi, Dr. Dima Farfurnik, and Dr. Robert Pettit. I would like to

recognize the support and assistance of all the members of the quantum photonics group; Dr. Kangmook Lim, Dr. Tao Cai, Dr. Jose Algarin, Dr. Shuo Sun, Dr. Zhili Yang, Zhouchen Luo, Aziz Karasahin, Sabyasachi Barik, Mustafa Atabey Buyukkaya, Subhojit Dutta, Yu Shi, Harjot Singh, Chang-Mu Han, Sam Harper, Shantam Ravan, Uday Saha, Yuqi Zhao, and Xinyuan Zheng. Thanks should also go to Alireza Seif and Chris Flower with whom I had great discussions. Thank you all for being great colleagues and friends.

I gratefully acknowledge the support from UMD nanocenter staff; John Abrahams, Jonathan A. Hummel, Tom Loughran, Mark Lecates, Wen-An Chiou, Sz-Chian Liou, and Jiancun Rao. They worked tirelessly to maintain the performance of the equipment and were always there for me when I needed their help. I very much appreciate the hard work of ECE and IREAP staff who helped me throughout these years; Vivian Lu, Bill Churma, Emily Irwin, Maria Hoo, Nolan Ballew, Bryan Quinn, Ed Condon, Nancy Boone, Dorothea Brosius, Don Schmadel, Taylor Prendergast, Shawn Fickes, Judi Gorski, and Leslie Delabar. Many thanks to Melanie Prange who always had a solution for any difficult circumstance. I also acknowledge the financial support from UMD's Wylie Dissertation Fellowship which helped me focus on writing the thesis in my last semester.

I am sincerely thankful to my parents and my sister who supported me with all their hearts from thousands of miles away. My friends in college park made this journey possible by being there for me outside of the lab when I needed to relax. Finally, I cannot begin to express my thanks to Leslie Minney, for all her support and encouragement in both good and bad days.

Table of Contents

List of Figures

List of Abbreviations

PIC	Photonic integrated circuit
InAs	Indium arsenide
InP	Indium phosphide
SOI	Silicon-on-insulator
CMOS	Complementary metal oxide semiconductor
$LiNbO_3$	Lithium niobate
SEM	Scanning electron microscope
FIB	Focused ion beam
MBE	Molecular Beam Epitaxy
SiO_2	Silicon oxide
FDTD	Finite-difference time-domain
Si	Silicon
SiN	Silicon nitride
GaAs	Gallium Arsenide
Ar	Argon
Cr	Chromium
Au	Gold
cQED	Cavity quantum electrodynamics

Chapter 1: Introduction

1.1 Overview

Quantum information science has attracted great attention in the past few decades for its promise of revolutionizing the current information processing capabilities in applications ranging from computing [1] and communications [2] to sensing . Photons (i.e., quanta of light) are a great candidate for encoding and transmitting quantum information due to their low noise and low-loss distant propagation. On the other hand, advances in Photonic Integrated Circuits (PICs) have helped develop many optical elements required for information processing on-chip. Optical elements based on PICs offer additional functionalities, increased robustness, compact footprint, and programmable performance compared to their bulk optical counterparts.

Exploiting the PIC technology for quantum applications is very promising and seems inevitable. With the increased size of quantum photonic experiments, realizing all the required elements with bulk optics will be extremely difficult and expensive. While classical and quantum photonic circuits share many of the building blocks, such as optical beam-splitters, phase shifters, etc., certain elements are unique to the quantum devices.

Figure 1 shows a schematic of a programmable photonic hardware that can implement quantum algorithms for quantum computation, communications, simulation, and sensing. Such a circuit consists of three major modules that are responsible for 1) generation 2) manipulation and 3) detection of non-classical light. The first module consists of deterministic single-photon emitters. By carefully designing the photonic structures this emission can be efficiently propagated to the low-loss optical waveguides. Next module contains linear and non-linear optical elements for manipulating the photons coupled to the waveguides. Combination of directional couplers (i.e., on-chip beam-splitters) and phase-shifters is enough to perform any unitary operation on the photons. For non-linear operations one can rely on optical non-linearities in the photonic platform or the non-linear nature of the light-matter interaction made possible with interfacing the photonic platform with single quantum emitters. Finally, after the linear and non-linear manipulation of the photons, sensitive detectors can measure the photons and determine the outcome of the experiment. In the following sections, each of these modules will be introduced and their material requirements will be discussed.

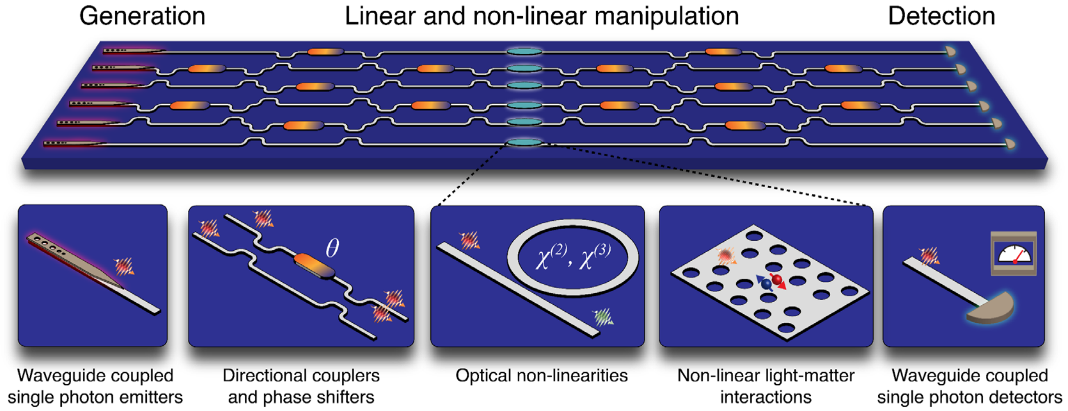

Figure 1. Schematic of a hybrid integrated quantum photonic circuit consisting of different modules for generation, linear and non-linear manipulation, and detection of non-classical light on a single chip.

1.2 Single-photon sources

First requirement for photonic implementation of quantum algorithms is a high-quality source of light that emit photons one at a time. Such an emission has a significantly different statistics compared with thermal or coherent light sources. There are three major criteria for a good single photon source [3]: a) High purity (i.e., ratio of the collected photons from the source that are single photons) b) High indistinguishability (i.e., wave-packet overlap between two photons generated from the source at different times) c) High brightness (i.e., number of single photons collected from the source divided by the number of times the source is triggered). Methods to measure these quantities will be discussed in the following chapters.

There are two common techniques for generating single photons: Probabilistic techniques based on non-linear optical processes such as spontaneous parametric down conversion and deterministic methods using quantum emitters [4]. Down conversion sources are limited in their quality due to the probabilistic nature of the light generation. There has been significant progress in improving their properties with various techniques, such as time-multiplexing [5], but those will not be the subject of this thesis. Quantum emitters are quantum objects like atoms, ions, molecules, and artificial atoms that emit single photons on-demand. Quantum emitters that are hosted in solids are particularly promising since there is no need for complicated active trapping unlike atoms or ions. Self-assembled and colloidal quantum dots [6,7], color centers in diamond and SiC [8], and defect centers in two-dimensional materials [9,10] are among the prominent examples of solid-state quantum emitters.

In this thesis, we have used Indium Arsenide (InAs) quantum dots hosted in Indium Phosphide (InP) which are bright indistinguishable sources of single photons in the telecommunications (telecom) wavelengths [11]. These quantum dots are specifically selected for their emission in the telecom band which is compatible with fiber optics networks.

1.3 PIC platforms

The backbone of the architecture illustrated in Figure 1 is a photonic integrated circuit that consists of low-loss optical waveguides, linear, and non-linear optical elements. There are several candidate material platforms for quantum PICs with their unique strengths and weaknesses. Silicon-on-insulator (SOI), for example, is the most mature material platform due to its compatibility with Complementary Metal-Oxide-Semiconductor (CMOS) technology and can be fabricated using the advanced foundry facilities previously developed for electronics. The high refractive index contrast between the silicon core and the silicon oxide cladding enables very small bending radius in this platform which means optical elements can be packed very efficiently in a small footprint. High-quality SOI waveguides also offer ultralow linear optical loss of the order of $2.7\ dB/m$ [12]. Chapters 2 and 3 describe our results based on low-loss SOI waveguides.

Another important criterion for a good quantum PIC is reconfigurability. Available methods for reconfiguring silicon-based photonics lose their efficiency at cryogenic temperatures which is where quantum emitters mentioned above have their best performance. One possible solution is to use materials with electro-optic effect such as lithium niobate ($LiNbO_3$) that can switch light at ultra-short time scales [13] even at cryogenic temperatures. Our experimental results using thin-film $LiNbO_3$ waveguides are described in Chapter 4.

1.4 Single-photon detectors

The third module of the quantum photonic circuit is sensitive detectors to measure the photons and identify the outcome of the experiment. Several schemes, such as grating couplers, fiber couplers, and edge couplers, can couple the photons off chip and route them to stand-alone detectors. However, these schemes can be alignment-sensitive and narrow-band. Ideally, single-photon detectors can be integrated on the same chip so that photons do not leave the chip from generation to detection. Superconducting nanowire single-photon detectors are particularly promising because of their superior detection properties (efficiency $> 90\%$, low dark count $< 1\ cps$, and low timing jitter $< 100\ ps$) [14] and their compatibility with photonic integrated circuits [15]. While these detectors are very promising, realizing them was not the focus of this thesis and we used traditional techniques for photon collection based on out-of-plane emission and grating couplers which will be discussed in the following chapters.

1.5 Hybrid integration

Each module of the quantum photonic circuits has unique material requirements. There are several candidate material platforms for each of the modules. A material that is good for generating non-classical light is not necessarily the best photonic platform to route and manipulate the generated photons. For example, silicon photonics is a great platform for routing and propagating photons, but generation of light in this platform is limited to probabilistic processes. On the other hand, quantum dots in III-V materials generate high-quality single photons on-demand but photonic elements based on III-V materials are not at the maturity level of silicon photonics. Therefore, an ideal quantum photonic circuit consists of a hybrid material platform where each element is made of the ideal candidate material.

There are several techniques to realize hybrid integrated quantum photonics with various degrees of complexity.

Figure 2 shows simple schematics of these techniques. The most straight-forward technique is to randomly disperse quantum emitters that are hosted in nanoparticles onto a pre-patterned photonic structure as shown in Figure 2a. This method allows rapid prototyping and the non-deterministic nature of the integration can be mitigated using patterned masks prior to deposition [16]. Another approach is to directly grow different materials on top of each other with epitaxial methods as shown in Figure 2b. While the film qualities in this method can be limited due to lattice mismatch in different layers, the possibility of realizing large area wafers makes this technique scalable for complex hybrid systems. Wafer bonding is another method that provides large scale devices made of different layers. Two dissimilar wafers are coated with thin layers that act as adhesive agent and by applying pressure to the stack of wafers a permanent bond will form between them [17].

Figures 2d and 2e show the principle for pick-and-place techniques using a transparent stamp [18] and a micro-probe [19], respectively. In contrast with the other methods, pick-and-place offers the unique possibility of nano-fabricating and processing each chip separately before integration which is crucial when the processing steps for one chip are incompatible or possibly harmful for the other chip. To realize hybrid integrated quantum photonics, in this thesis, we have used the pick-and-place using a micro-probe which will be described in detail in the following section.

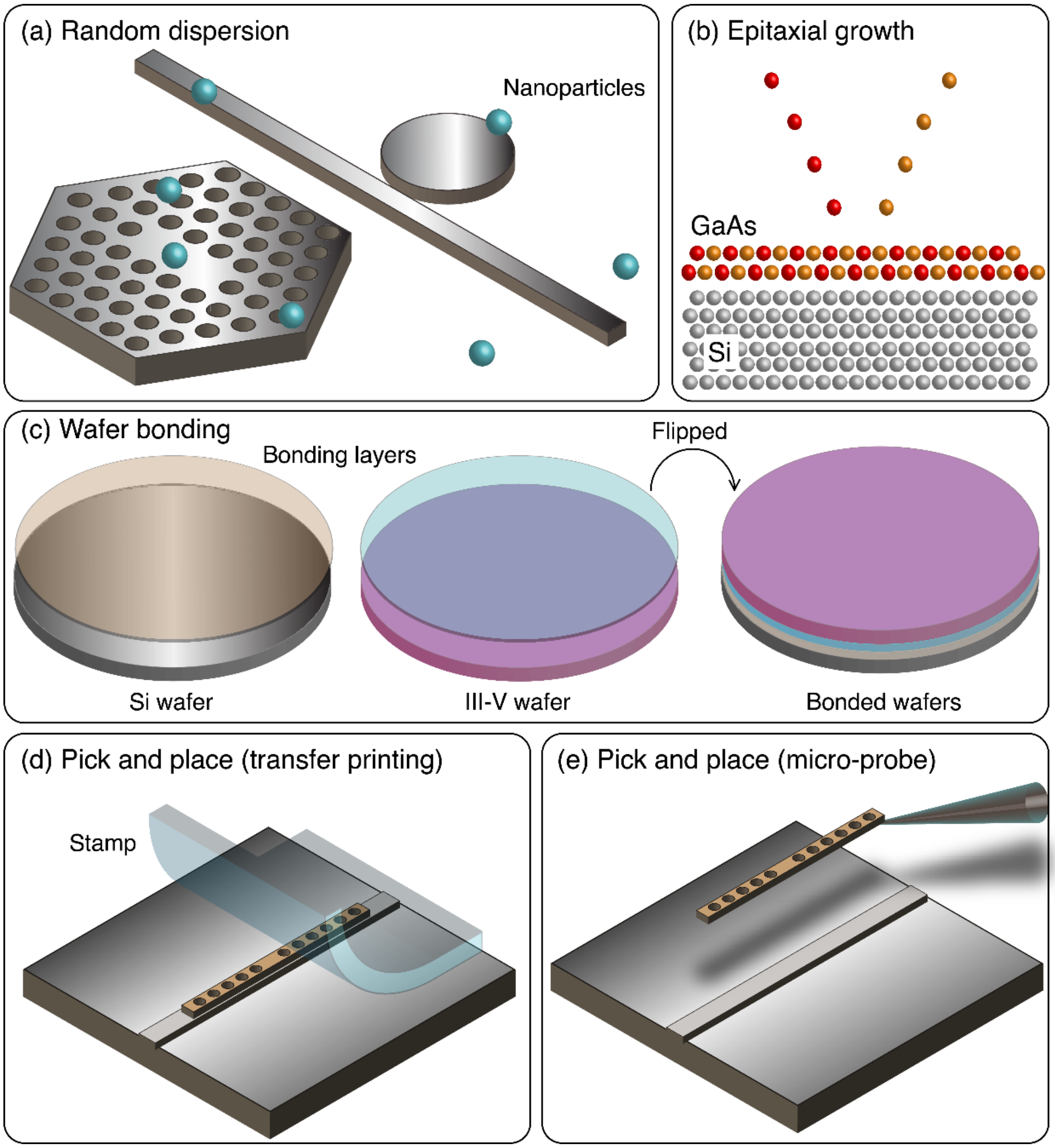

Figure 2. Schematics of various hybrid integration methods for the quantum emitters on the photonic platforms. (a) Randomly dispersed nanoparticles in the vicinity of photonic structures such as a microdisk or a photonic crystal cavity. (b) Epitaxially grown GaAs layer on a Si substrate with a buffer layer (not shown). (c) Wafer-bonding technique to form a heterostructure of a III-V layer on a Si substrate. (d) Transfer printing process of the nanobeam including quantum emitters on a waveguide using a rubber stamp. (e) Pick and place process using a microprobe that places the emitter on a waveguide.

1.6 Micro-probe assisted pick-and-place technique

We perform the pick-and-place process in a scanning electron microscope (SEM) system combined with a focused ion beam (FIB) and a microprobe manipulator. To separate the nanobeam devices from the substrate, first we cut two of three thin tethers using focused ion beam and contact the probe on the nanobeam device (see Figure 3). Next we cut the remaining tether of the device using the FIB which fully separates the nanobeam from the substrate. The sample adheres to the tip by van der Waals force. We then move the nanobeam to the target chip and place the device on the pre-patterned photonic waveguides. We place the nanobeam with scanning electron microscope resolution, and thus we could deterministically integrate the nanobeam onto the target photonic circuit. This procedure takes approximately one hour to place the nanobeam in the correct position on or by the side of the waveguide.

1.7 Fabrication of suspended nano-structures in InP

Quantum dots are grown using molecular beam epitaxy (MBE). InAs quantum dots have a density of approximately $10\ \mu m^{-2}$ in a 280 nm thick InP membrane on a 2 μm thick sacrificial layer. We pattern the nanobeam device using electron beam lithography followed by inductively coupled plasma reactive ion etching and used a chemical wet etch (H2O/HCl/H2O2 = 3:1:1) to remove the sacrificial layer leaving a suspended beam supported by several thin tethers. The nanobeam has a width of 500 nm and tapered length of 5 μm and includes a Bragg mirror consisting of air hole arrays with a radius of 100 nm and pitch of 350 nm.

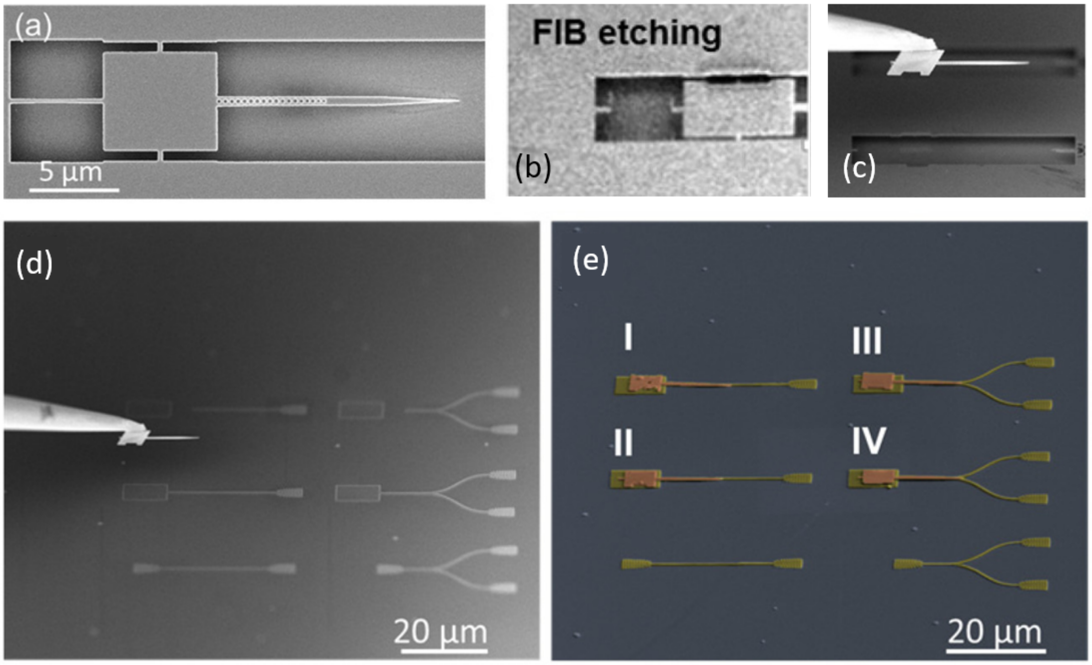

Figure 3. Micro-probe assisted pick-and-place process. Adopted from [20] (a) Suspended nano-structure in InP (b) Etching two out of three support tethers using focused ion beam. (c) Picking the nanostructure with the micro-probe and etching the last support tether. (d) Moving the nano-beam to the target wafer (e) Successful placing of several nano-beam on the target waveguides and beam-splitters.

1.8 Micro-Photoluminescence measurement setup

We characterize our devices in a low temperature micro-photoluminescence setup. A low vibration closed cycle cryostat (Montana Instruments) cooled the sample down to 4 K. To measure the photoluminescence emission spectrum of the quantum dots, we used a 780 nm continuous wave or a 785 nm pulsed laser for excitation. We excited the quantum dots and collected the photoluminescence signal using an objective lens (NA = 0.7, 100x) and a spectrometer (Princeton Instrument). For the second-order correlation measurement, we measured the photon coincidences using two superconducting nanowire single photon detectors (Quantum Opus) operated at 3.2 K. The detectors had a dark count of 150 counts/s.

1.9 Thesis outline

In chapter 2, we demonstrate coupling of single-photon emitters embedded in InP nanostructures with silicon photonics. We use an on-chip beamsplitter to perform photon-correlation measurements in order to confirm the single-photon nature of the emission. In chapter 3, we describe design, fabrication, and measurement of an on-chip silicon photonic add-drop filter for quantum emitters that can route and filter quantum dot emission. Chapter 4 covers the integration of quantum dot single photons to thin-film lithium niobate photonics. In chapter 5, we report design, simulation, and fabrication of a electrostatic capacitive device that can tune the emission energy of quantum dots using quantum confined Stark effect. In chapter 6, we demonstrate optical amplification of weak probe signals with a single quantum dot strongly coupled to a photonic crystal cavity. We conclude and discuss the future directions in chapter 7. Parts of this dissertation has been previously published in the following articles:

Chapter 1:

> Kim, J.H., Aghaeimeibodi, S., Carolan, J., Englund, D. and Waks, E., 2019. Hybrid integration methods for on-chip quantum photonics. arXiv preprint arXiv:1911.12756 [21].

Chapter 2:

> Kim, J.H.*, Aghaeimeibodi, S.*, Richardson, C.J., Leavitt, R.P., Englund, D. and Waks, E., 2017. Hybrid integration of solid-state quantum emitters on a silicon photonic chip. Nano letters, 17(12), pp.7394-7400 (*equal contribution) [20].

Chapter 3:

Aghaeimeibodi, S., Kim, J.H., Lee, C.M., Buyukkaya, M.A., Richardson, C. and Waks, E., 2019. Silicon photonic add-drop filter for quantum emitters. Optics Express, 27(12), pp.16882-16889 [22].

Chapter 4:

Aghaeimeibodi, S., Desiatov, B., Kim, J.H., Lee, C.M., Buyukkaya, M.A., Karasahin, A., Richardson, C.J., Leavitt, R.P., Lončar, M. and Waks, E., 2018. Integration of quantum dots with lithium niobate photonics. Applied Physics Letters, 113(22), p.221102 [23].

Chapter 5:

Aghaeimeibodi, S., Lee, C.M., Buyukkaya, M.A., Richardson, C.J. and Waks, E., 2019. Large stark tuning of InAs/InP quantum dots. Applied Physics Letters, 114(7), p.071105 [24].

Chapter 2: Integration of quantum emitters with silicon photonics

2.1 Introduction

Silicon (Si) has many advantages as a material for integrated quantum photonic devices. It has a large refractive index that enables many photonic components to fit into a small device size [25,26]. Silicon is also compatible with standard CMOS fabrication methods that can combine electronics with photonics on a large scale [27]. Therefore, silicon photonics can achieve the most complex integrated photonic structures to date composed of thousands of optical components in a single chip [28]. However, silicon is an indirect bandgap material with poor optical emission properties. The most common approach for generating single photons in silicon is to exploit the third-order nonlinearity to create entangled photon pairs by down-conversion [29]. But these sources only generate heralded single photons and extending them to an on-demand source by multiplexing remains a significant challenge. To date, the incorporation of on-demand single photon sources on a silicon photonic chip remains a difficult challenge.

In this chapter, we demonstrate the integration of silicon photonic devices with a solid-state single-photon emitter. We use a hybrid approach that combines silicon photonic waveguides with InAs/InP quantum dots that act as efficient sources of single photons at telecom wavelengths spanning the O-band and C-band [11,30,31]. A pick-and-place technique allows transferring of tapered InP nanobeams containing InAs quantum dots onto a silicon waveguide with nanometer-scale precision. The tapered nanobeams efficiently couple the emission from the quantum dot to the silicon waveguide. The fabricated devices exhibit clear single-photon emission, which we validate via photon correlation measurements using an on-chip beamsplitter. Our approach could enable deterministic fabrication of complex circuits composed of multiple single photon emitters coupled to large-scale silicon photonic devices.

2.2 Design and simulation of the hybrid structure

Figure 4a shows a schematic of the heterogeneous integration by placement of a thin InP nanobeam on top of a silicon ridge waveguide. The quantum dots have an emission wavelength around 1300 nm, measured in a bulk sample at 4 K. This wavelength is well below the bandgap of silicon, ensuring that the emitted photons will experience low absorption losses. The InP nanobeam has a width of 500 nm and a thickness of 280 nm while the silicon waveguide has a width of 400 nm and a thickness of 220 nm on the 3 μm thick silicon oxide (SiO_2) layer on top of a silicon. We taper the nanobeam with a tapered angle of 6° and a tapered length of 5 μm in order to adiabatically convert the photonic mode from the InP beam to the silicon waveguide.

To estimate the coupling efficiency between the nanobeam and waveguide, we simulate the mode propagation in the integrated structure using a finite-difference time-domain (FDTD) numerical simulation. We approximate the quantum dot emission with a dipole source located at the center of the nanobeam. Figure 4b shows the magnitude of the electric field generated by the dipole as it propagates through the tapered region. Near the center of the beam, the emission from the dipole couples to both the InP nanobeam and the Si waveguide due to their similar refractive indices of 3.2 and 3.5, respectively. But as the nanobeam tapers, the field adiabatically transforms to the single mode of the silicon waveguide, as shown in the transverse mode profiles in Figure 4b taken at several positions along the taper. In the simulation, we assume that the quantum dot emission propagates only in one direction and calculate a 32% coupling efficiency from the dipole to the silicon waveguide mode while a non-tapered nanobeam has a lower coupling efficiency of 13% due to scattering and back-reflection at the end of the nanobeam as shown in Figure 5.

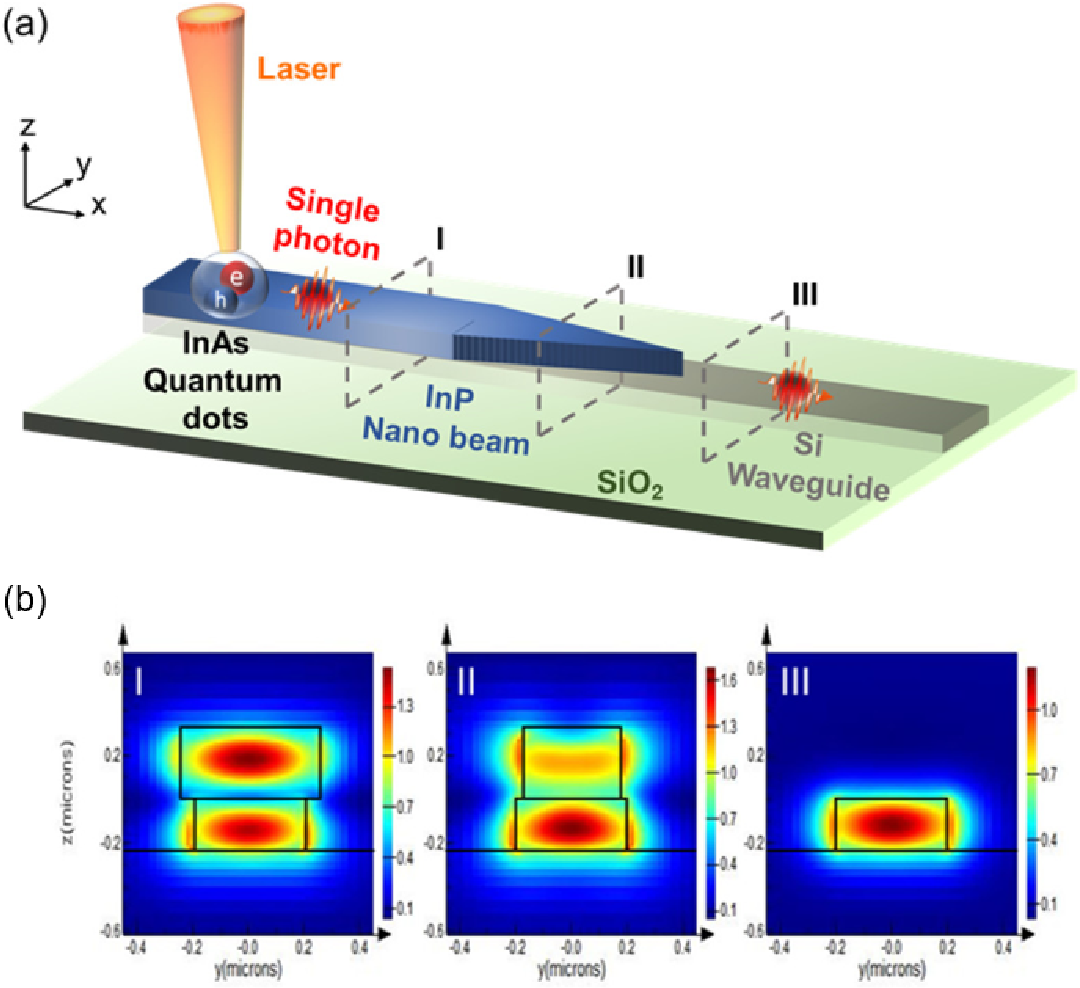

Figure 4. Schematic of the integrated InP nanobeam and silicon waveguide. (b) Simulated electric field (|E|) profiles at different cross-sectional positions of I, II, and III marked in (a). Black lines represent the boundary of the structures.

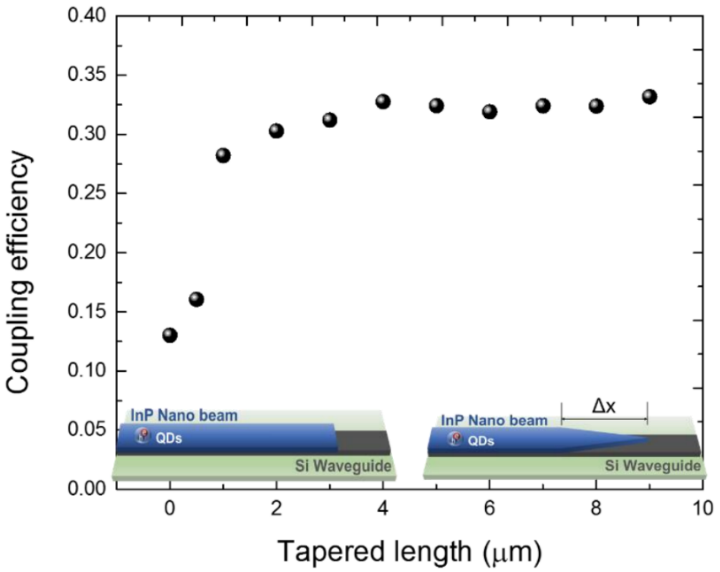

Figure 5. Coupling efficiency as a function of the InP nanobeam taper length.

2.3 *Fabrication and pick-and-place procedure*

We fabricate the InP nanobeam using the method described in 1.7. We also fabricate the silicon waveguide separately using electron beam lithography and dry etching. Figure 6a shows a scanning electron microscope image of the fabricated nanobeam that is suspended by thin tethers that attach it to the bulk substrate. The nanobeam contains a periodic array of air holes on one end that acts as a Bragg mirror to direct the quantum dot emission in one direction. Figure 6b shows a scanning electron microscope image of a fabricated silicon photonic waveguide. A grating coupler on one end of the device couples the emission from the waveguide to the out-of-plane for detection. The grating structure efficiently out-couples the transverse-electric mode with a coupling efficiency of 37% while the transverse-magnetic mode has a low coupling efficiency of 3%. These values are obtained from three-dimensional FDTD simulations. We also fabricate a y-shaped waveguide acting as a 50-50 on-chip beamsplitter as shown in Figure 6c. The square pad on the left end of the nanobeam and waveguide facilitates picking and placing the nanobeams as described in 1.6.

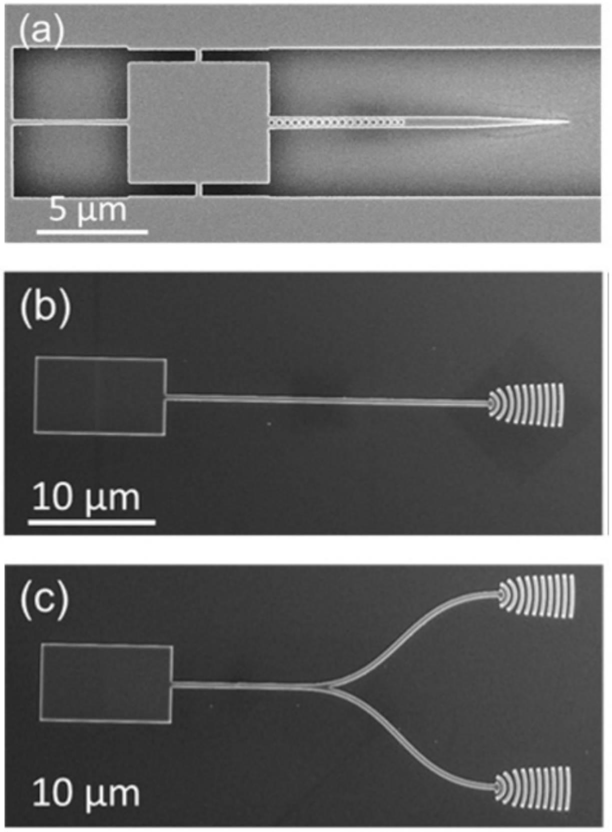

Figure 6. (a) SEM image of the fabricated tapered nanobeam containing InAs quantum dots. (b,c) SEM images of the fabricated silicon (b) straight waveguide and (c) y-shaped 50-50 waveguide beam splitter.

Figure 7 shows a SEM image of four completed devices composed of integrated nanobeams on silicon waveguides using the pick-and-place technique described in 1.6. The fact that we can integrate a nanobeam on each structure in the 2 × 2 array of waveguides demonstrates the repeatability and high yield of this procedure.

2.4 Device characterization

We use a low temperature (4 K) micro-photoluminescence setup to characterize the integrated devices as described in 1.8. We excite the quantum dots using a 780 nm continuous wave laser and collect the signal from the grating out-coupler. All the integrated devices in Figure 7 are optically functional and show multiple single quantum dot emissions through the grating coupler.

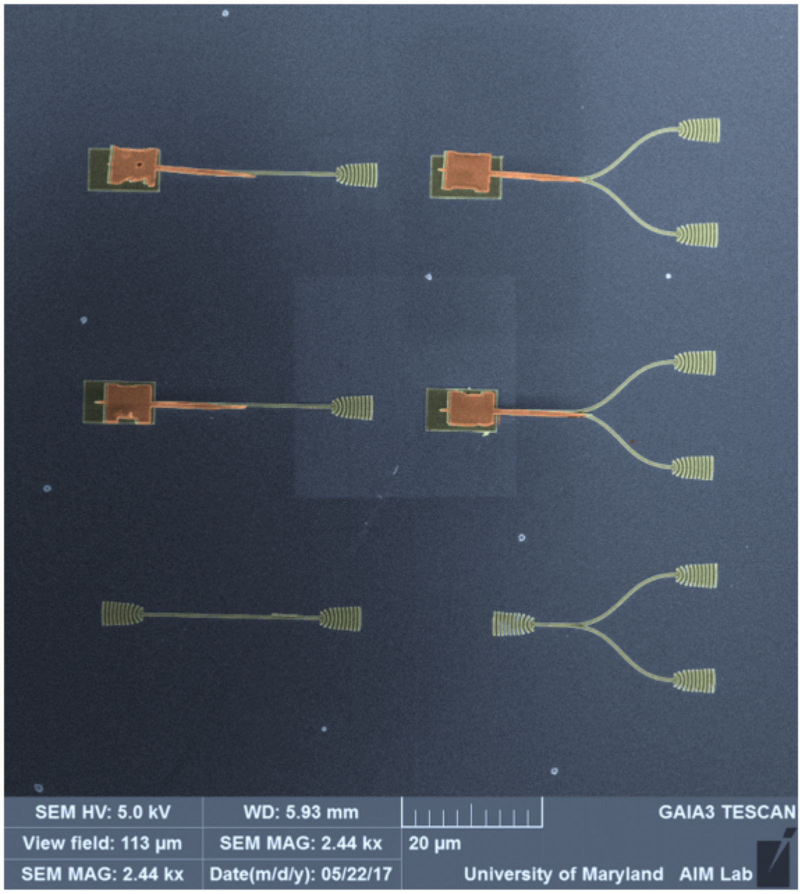

Figure 7. False-color SEM image of the integrated nanobeam and silicon waveguide devices. Red, yellow, and navy colors indicate InP nanobeam, silicon waveguides, and SiO_2 top surface, respectively.

Figure 8 shows the resulting photoluminescence spectrum obtained from one of the straight waveguide devices. We observe multiple sharp peaks corresponding to single quantum dots, demonstrating that the emission from the quantum dots coupled to the waveguide mode. The quantum dot emissions from the grating show a factor of 4 increase in intensity as compared to that of the quantum dots in a bulk sample, experimentally confirming our numerical predictions.

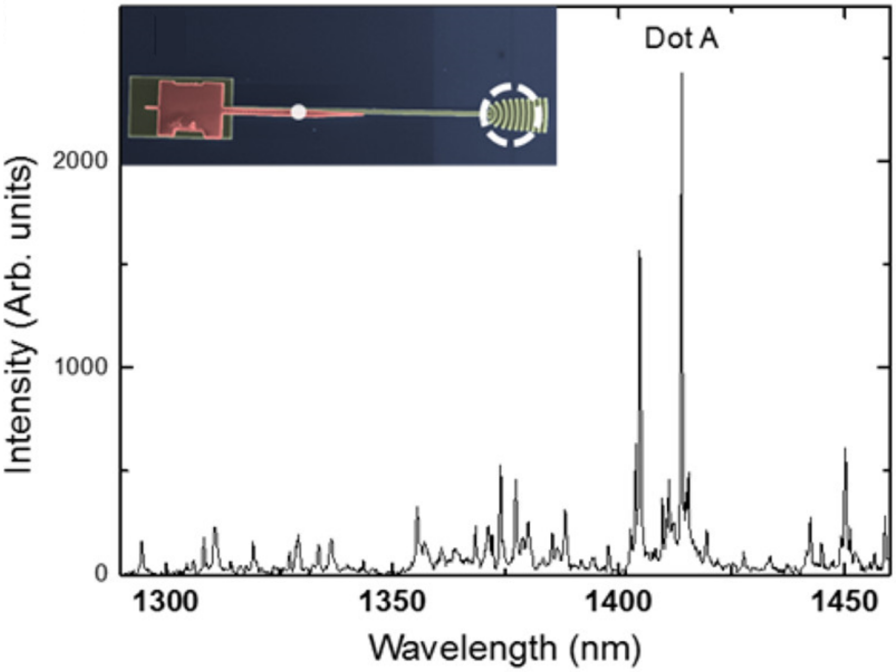

Figure 8. (a) Photoluminescence spectrum of the quantum dots on a straight silicon waveguide. Inset show the excitation and the collection scheme where the white dot is excitation spot and the dashed white circle is the collection area.

To estimate the brightness of the waveguide-coupled quantum dots, we excite the quantum dots with a 40 MHz pulsed laser and measured the photon counting rate of 10.8 kHz at the single photon detector. On the basis of our spectroscopy system efficiency of 0.85%, including a transmission efficiency of optics (35%) and spectrometer (38%), fiber coupling efficiency to the detector (32%), and the detector quantum efficiency (20%), we determined a collection efficiency of 3.2% at the first lens for the measured quantum dot A in Figure 8. This efficiency is lower than the expected ideal efficiency of 11.8%.

We calculated the collection efficiency of the emission quantum dots at the first lens (NA = 0.7) using a finite-difference time-domain simulation. A dipole source at the center of the nanobeam mimics the quantum dots in the simulation. From this simulation, we calculated the coupling efficiency of 71% from the quantum dots to the integrated nanobeam and waveguide structure, the coupling efficiency of 45% from the integrated structures to the silicon waveguide, and the out-coupling efficiency of 37% at the grating coupler, resulting in a total collection efficiency of 11.8% at the first lens. In the simulation, we assumed that the quantum dot emission propagates only in one direction.

One reason for this degraded efficiency is an imperfect reflection from the Bragg mirror. From the simulation, we calculate that the Bragg mirror sitting on a silicon waveguide reflects only 30% of the incident light, as compared to the Bragg mirror in air which reflects 95% of the light. Another reason for the low efficiency could be the dipole orientation of quantum dots, which may not be perfectly aligned with the TE mode of the waveguide. The nonideal position of the quantum dot within the nanobeam and the positional and rotational mis-alignment between the nanobeam and waveguide could further degrade the efficiency.

From numerical simulations, we determined that the coupling efficiency drops by half when the quantum dots are displaced from the center of the nanobeam by 130 nm (Figure 9a). We also calculate that the efficiencies drop by half when the nanobeam has a displacement of about 400 nm from the center of the silicon waveguide (Figure 9b) or is rotated about 10° (Figure 9c).

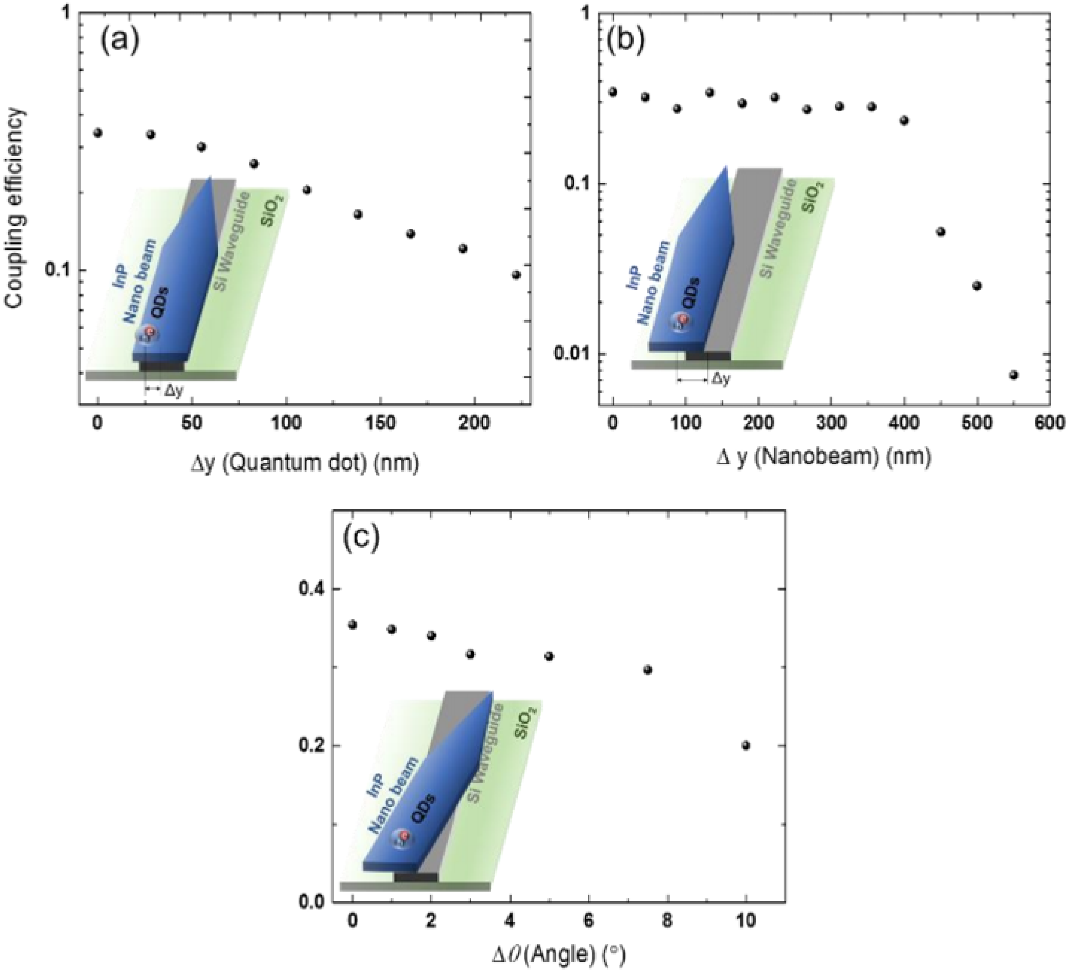

Figure 9. Coupling efficiency as a function of (a) the distance of the quantum dot from the center of the nanobeam. (b) The distance of the nanobeam center from the silicon waveguide center. (c) relative angle between the nanobeam and the silicon waveguide.

These simulations indicate that the alignment tolerances between the nanobeam and waveguide are relatively mild, and we could achieve these alignment accuracies between the nanobeam and waveguide. Finally, fabrication errors also reduce the coupling efficiency. In particular, we observe that the fabricated grating teeth has a width of 295 nm larger than the ideal value of 275 nm. This fabrication error reduces the out-coupling efficiency of the grating from 37% to 25% as shown in the Figure 10.

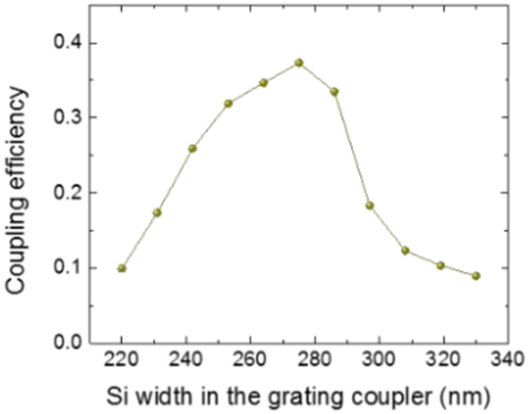

Figure 10. Grating coupler efficiency for the transverse electric mode as a function of the silicon width.

2.5 On-chip photon statistics measurement

In this section, we investigate the device shown in Figure 7 that integrates the nanobeam with an on-chip beamsplitter. Figure 11 plots the collected photoluminescence from top and bottom grating couplers when we excite the quantum dots near the center of the nanobeam. Each spectrum shows multiple sharp peaks corresponding to different quantum dots. We identify 16 independent resonant peaks, which we label in the figure. Each peak appears in both spectra, verifying that they originate from the same source. We independently measure the splitting ratio of the beamsplitter by sending a 1304 nm laser into the waveguide and comparing the intensities at the two gratings, giving a balanced splitting ratio of 43-57 as shown in Figure 12.

The beamsplitter structure allows direct measurements of the second-order correlation to confirm the single photon nature of the quantum dot emission. We send the collected light from each grating coupler to separate spectrometers using a pickoff mirror in order to filter the single quantum dot emission, and then couple the filtered signal to a single-photon detector (See 1.8).

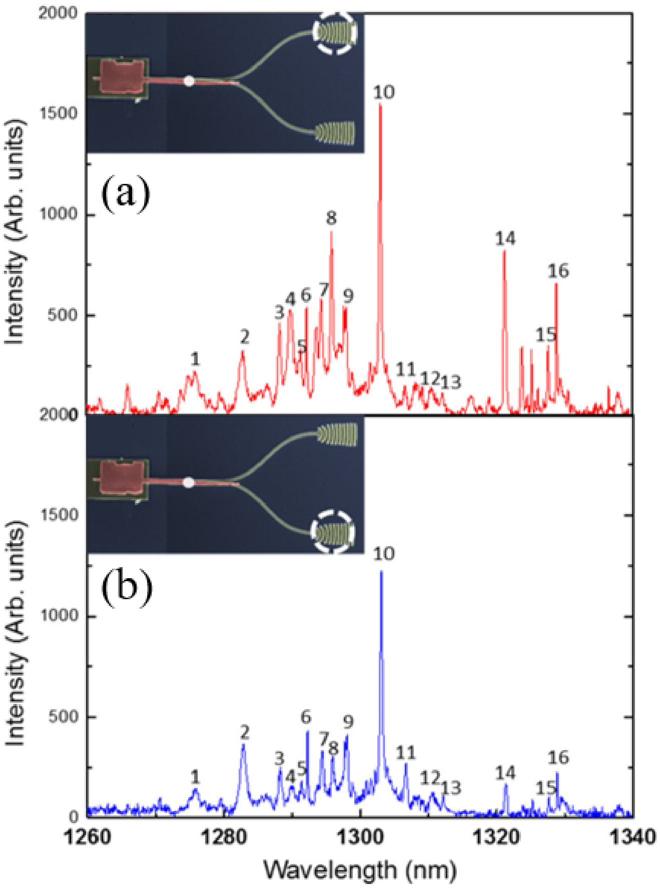

Figure 11. Photoluminescence spectrum of the quantum dots on a 50-50 on-chip beamsplitter collected at the (a) top grating and (b) bottom grating. Inset shows the excitation and collection scheme similar to the inset of the Figure 8.

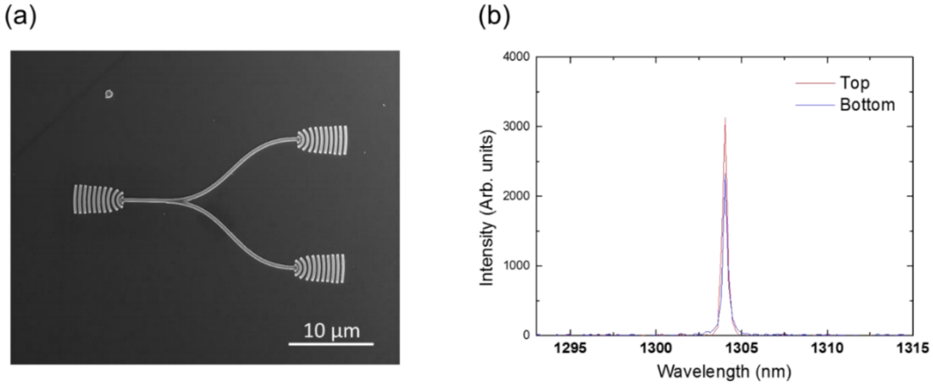

Figure 12. (a) SEM image of on-chip silicon beamsplitter with input and output gratings. (b) Measured laser signals from top and bottom grating couplers.

Figure 13a shows the measured second-order correlation function $g^{(2)}(\tau)$ from the quantum dot line 10 labeled in Figure 11 using the 50-50 waveguide beamsplitter after detector dark count subtraction. We have used a 780 nm continuous wave laser for this measurement. We fit the antibunching dip to the equation below:

$$g^{(2)}(\tau) = 1 - \left(1 - g^{(2)}(0)\right) \exp(-|\tau|/\tau_0)$$

To account for the limited detector time resolution (200 ps), we deconvolve the data with a Gaussian function and obtain $g^{(2)}(0) = 0.33$, which is below the classical limit of 0.5. We also perform the same experiment with a pulsed laser having a 40 MHz repetition rate shown in Figure 13b and observe $g^{(2)}_{pulsed}(0) = 0.25$, which was obtained by the ratio of the measured counts at the center peak divided by the average of the neighboring peaks.

We attribute the residual multiphoton events (i.e., imperfect single photon purity) to residual background emission due to above-band pumping. This contribution could be fully eliminated using resonant [32–34] or quasi-resonant [35] excitation.

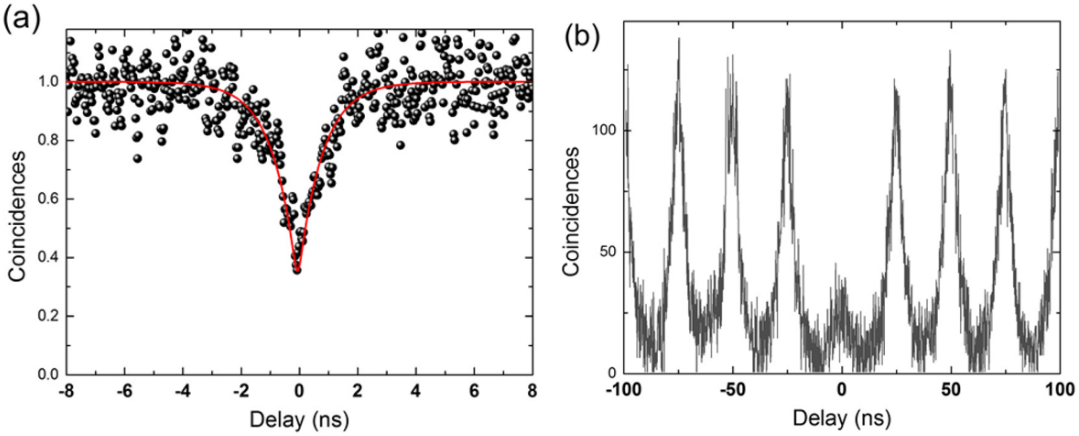

Figure 13. Second-order correlation histogram of the single quantum dot emission (line 10 in Figure 11) on the waveguide beamsplitter. (a) Continuous wave laser excitation and (b) pulsed laser excitation. Red solid-line in (a) is a fitted curve for $g^{(2)}(\tau)$.

2.6 Summary and discussions

In summary, in this chapter, we have demonstrated the deterministic integration of solid-state quantum emitters with silicon photonic devices. This integration opens up the possibility to leverage the highly advanced photonics capabilities developed in silicon to control and route nonclassical light from on-demand single photon sources. An example of a more complicated silicon photonics device will be described in the following chapter.

In addition, the fabricated devices operate at telecom wavelengths which are useful for fiber-based quantum communications. In the current device, the grating couplers are the most significant source of loss. Improved grating couplers using partial etching can achieve the out-coupling efficiency higher than 92% [36]. Alternatively, collecting photons from the edge of the chip [37], tapered fiber coupling [38], or integrating detectors directly on the photonic chip [15,39] would significantly improve the overall efficiency as previously discussed in 1.4.

Incorporation of site-controlled quantum dot growth [40,41] could further improve coupling efficiency of the emission to the waveguide by placing dots precisely in the nanobeam center and could improve the device yield when utilizing small mode-volume cavities. Ultimately, quantum photonic devices will require methods to couple multiple identical quantum emitters on different waveguides. Such integration is difficult to scale using direct growth or wafer-bonding methods due to randomness in the quantum dot positions and emission wavelengths. Pick-and-place could solve these problems by pre-characterizing fabricated quantum dot devices to select and then transfer only the ones that contain a quantum emitter with the desired properties. Local tuning methods based on temperature [42], strain [43], and quantum confined Stark effect [44] could provide additional fine-tuning to compensate for small residual spectral mismatch as well as to control on-chip interactions. We demonstrate this tuning in chapter 5 using quantum confined Stark effect.

Our results represent an important step toward complex quantum photonic circuits that could process many photons on a chip to simulate complex chemical reactions [45] and implement photonic quantum computation [1,46,47].

Chapter 3: On-chip filtering and routing of photons using silicon photonics

3.1 Introduction

Single photons are excellent carriers of quantum information and can be generated efficiently using quantum emitters [4]. Major advances have been made to integrate such high-quality single photon sources with low loss silicon-based optical waveguides. For example, several works have demonstrated the integration of solid-state quantum emitters with SiO_2 [48], silicon nitride (SiN) [19,49–52], and Si photonic chips [20,53]. We discussed an example of these efforts in the last chapter. Moreover, recent advances in developing on-chip single-photon detectors [39,54,55], have paved the way for quantum photonic circuits that are fully chip-integrated. Integrating these elements on the same chip enables compact quantum devices with robust and low loss operation as well as programmable functionality.

In addition to the generation and detection of photons, researchers have demonstrated different approaches for on-chip routing of single photons in the near infrared regime. The electro-optic effect [56] and optomechanical forces [57] of GaAs have been used to demonstrate routing of single photons in suspended structures containing quantum dots. Implementing single photon routing using silicon-based photonics rather than suspended GaAs waveguides could enable easier scaling because of the mature foundry-level fabrication available for this platform. A hybrid platform based on SiN waveguides and quantum dots hosted in GaAs has been used to implement routing and multiplexing of single photons in the near infrared regime [50].

However, SiN does not support fast reconfiguration mechanisms, which limits the ability to control the active filters in this platform to slow thermo-optic [50] or strain [58] tuning of the refractive index. In contrast, silicon photonics offers fast tuning by modulation of the carrier concentration using electrical contacts [59,60] or by introduction of field-induced second order nonlinearity [61]. To date, compact devices for routing and filtering quantum emitters with silicon photonics has yet to be implemented.

In this chapter, we demonstrate a silicon photonic add-drop filter that can filter and route telecom emission from single quantum dots. We use InAs quantum dots embedded in an InP nanobeam as bright sources of single-photon emission at the telecom band similar to chapter 2. This emission efficiently couples to a silicon waveguide using an adiabatic taper. The filter is comprised of an ultracompact silicon microdisk resonator that is evanescently coupled to waveguides [62]. We used the pick-and-place technique described in 1.6 to experimentally realize this hybrid structure. We demonstrate on-chip filtering of the unwanted background emission over a wide wavelength range while the desired quantum dot emission is efficiently transmitted through the filter. Moreover, by temperature tuning the system we can control the emission wavelength of a quantum dot with respect to that of the resonator and demonstrate routing of the emission between the drop and through channels. We also show tunability of the cavity resonance by direct laser heating the device. Filtering and routing single quantum dot emission in silicon photonics is an important step toward fully integrated quantum photonic circuits that generate, process, and detect light on a compact chip.

3.2 Device design

Figure 14a shows the general working principle of our proposed hybrid device, which features an InP nanobeam embedded with InAs quantum dots as well as a silicon microdisk resonator. Emission from the quantum dot couple to the transverse electric mode of the InP nanobeam. A Bragg reflector (period of 290 nm and radius of 100 nm) on one end of the nanobeam directs the photons in a single direction. An adiabatic taper on the other side of the InP nanobeam efficiently transfers the emission to the silicon waveguide, which is also tapered to match the optical mode of the nanobeam. Both tapers in the coupling region are 5 μm long.

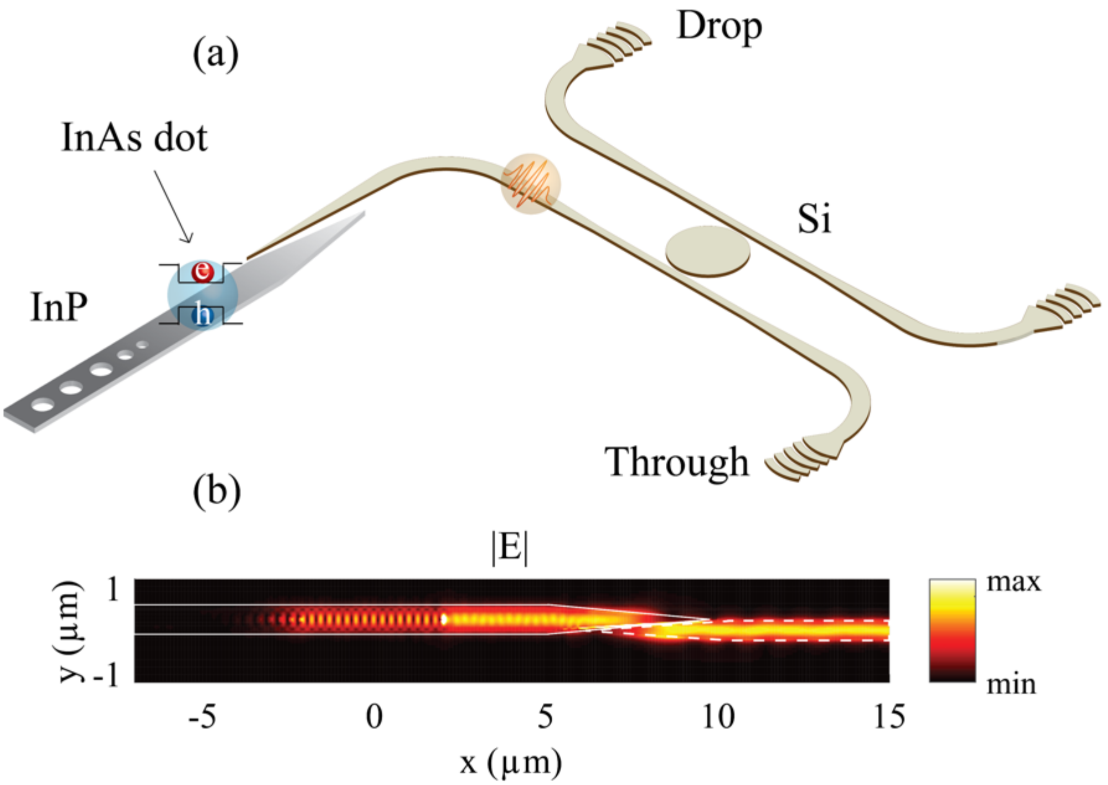

Figure 14. (a) Illustration of the hybrid device containing InAs quantum dots embedded in an InP nanobeam and a silicon photonic microdisk resonator. (b) Simulated light propagation in the coupling region.

The add-drop filter consists of a silicon microdisk resonator and two waveguides (drop and through channels) evanescently coupled at the top and bottom of the microdisk. Telecom photons from the quantum dot that are transferred to the silicon waveguide are routed to the drop channel if resonant with the microdisk. Otherwise, they propagate to the through channel of the add-drop filter. By tuning the wavelength of either the quantum dot or the microdisk resonator we can essentially switch the quantum dot emission between the drop and through channels.

Figure 14b shows the simulated propagation of light at the intersection of the InP nanobeam and the silicon waveguide when they are placed side by side. Using a finite-difference time-domain simulation (Lumerical, FDTD), we calculated a coupling efficiency exceeding 95% at 1300 nm, which is the typical emission wavelength of our quantum dots.

We performed variational finite-difference time-domain simulations (Lumerical, Mode) to design the resonance wavelength and linewidth of the resonator. Linewidth of our quantum dots in nanobeam structures are ~0.1 nm (70 μeV) for the narrowest emission lines. We note that quantum dots in bulk show a slightly narrower linewidth, but still broader than more developed InAs/GaAs quantum dots. Figure 15 shows the statistical study of linewidth of 100 quantum dots (50 in bulk and 50 in nanobeams).

Considering the linewidth of our quantum dots, a quality factor larger than 1000 for the microdisk resonator is not desirable for achieving efficient transfer of the photons to the drop channel due to losses from filtering the quantum dot emission spectrum. To maintain a small footprint, we used a disk radius of 2.125 μm, gap of 90 nm between the drop/through channels and microdisk, and a waveguide width and height of 230 nm and 220 nm, respectively. From simulation using these parameters, we obtained a resonance of around 1300 nm with a quality factor of 620.

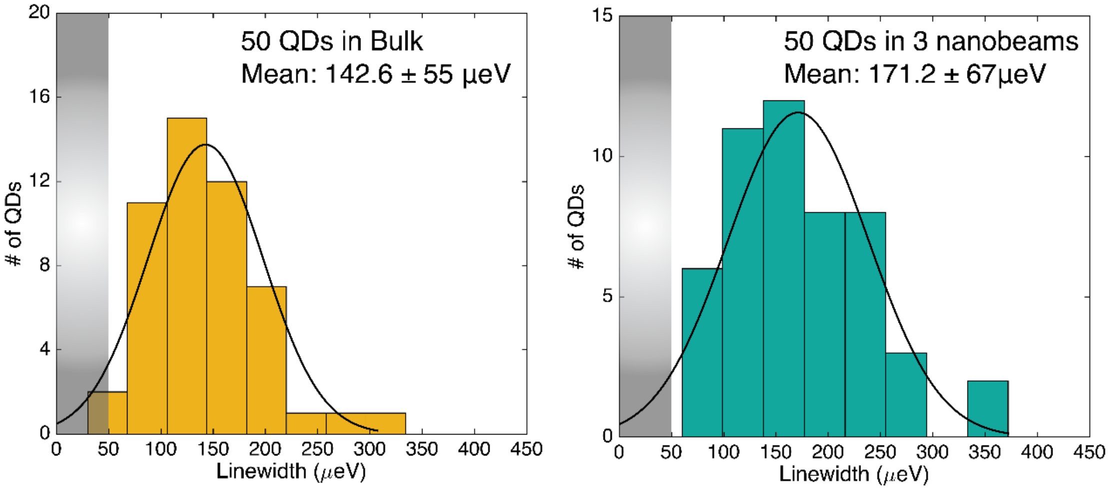

Figure 15. Statistical histogram of the quantum linewidth in (left) bulk (right) nanobeams. Gray shaded areas show the spectrometer resolution limit.

Figure 16 a and b show the simulated transmission of light to the through and drop channels, respectively. The silicon waveguide width at the curves is 400 nm to avoid additional bending losses. The width tapers down to 230 nm to match the optical mode of the disk resonator over a length of 5 µm. Both drop and through channels end with periodic grating couplers (550 nm period and 50% duty cycle) with a 37% outcoupling efficiency for the transverse electric mode. We calculated a total efficiency of 29% which consists of quantum dot to InP coupling (93%), InP to Silicon transmission (95%), microdisk transmission to the drop channel (89.7%), and grating outcoupling efficiency (37%). This theoretical value of the coupling efficiency is comparable to that of the device in chapter 2, although the device in this chapter is more complicated.

3.3 Device fabrication and characterization

The device fabrication and the pick-and-place procedure for the suspended InP nanobeams are described in 1.7 and 1.6, respectively. We chose a 220 nm thick silicon-on-insulator substrate to define our add-drop filter and used electron beam lithography to pattern the resist. Then we deposited Cr as a metal mask. Finally, we etched the substrate with inductively coupled plasma etching and removed the Cr. Although fabrication of resonator devices with gaps as low as 90 nm is challenging, our fabricated devices indicate a reasonable repeatability as shown in Figure 17 demonstrating our control over the geometry of the disk and the gap.

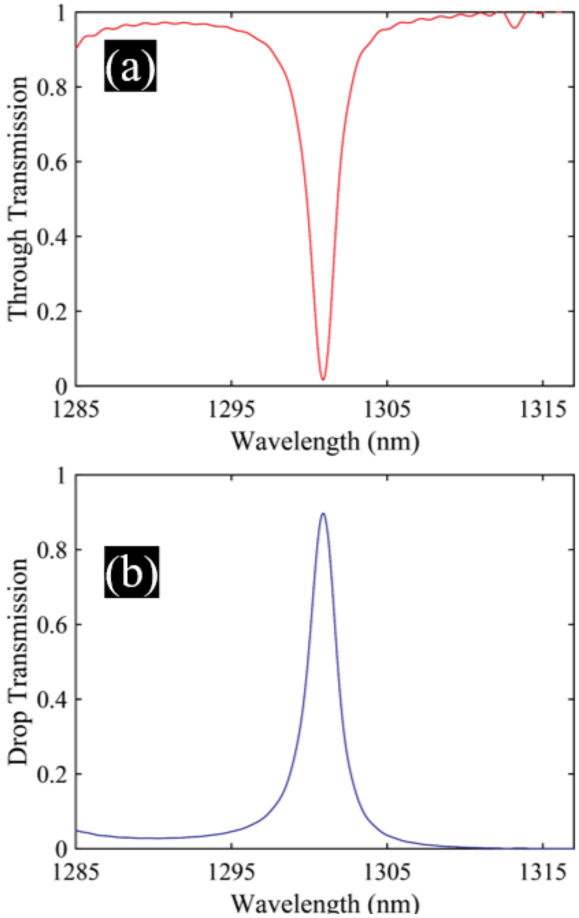

Figure 16. Simulated transmission of light to the (a) through and (b) drop channels of the add-drop filter.

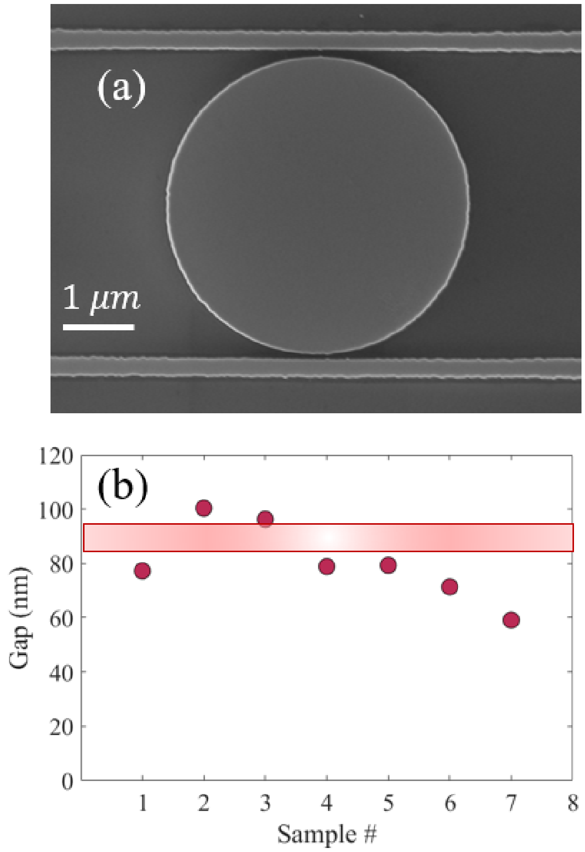

Figure 17. (a) SEM image of the fabricated disk resonator. (b) measured gap distance for several fabricated devices showing repeatability. The dashed red box indicates the desired 90 nm gap.

Figure 18a shows a false color SEM image of the integrated device after the pick-and-place. Figure 18b is a further magnified view of the coupling region where the InP and silicon tapered waveguides are placed side-by-side. To characterize the response of the microdisk resonator (see 1.8 for details), we used the broad emission of the ensemble quantum dots, which had an inhomogeneous broadening of more than 200 nm [63]. Therefore, at high excitation powers (orders of magnitude higher than the saturation power of the quantum dots) they act as integrated broadband light sources.

By collecting the photoluminescence signal from the drop and through channels and normalizing by the total signal, we obtained the response of the microdisk resonator. Figure 19a and 19b show the transmission spectra of the through and drop channels respectively, when we excited the nanobeam with a power of 520 μW.

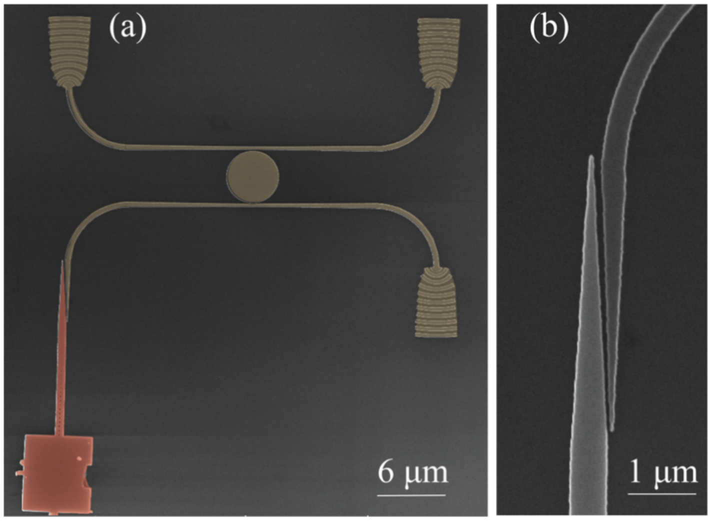

Figure 18. (a) False color SEM image of the fabricated hybrid device. Red and yellow represent InP and silicon, respectively. (b) A magnified view of the adiabatic tapering in the coupling region.

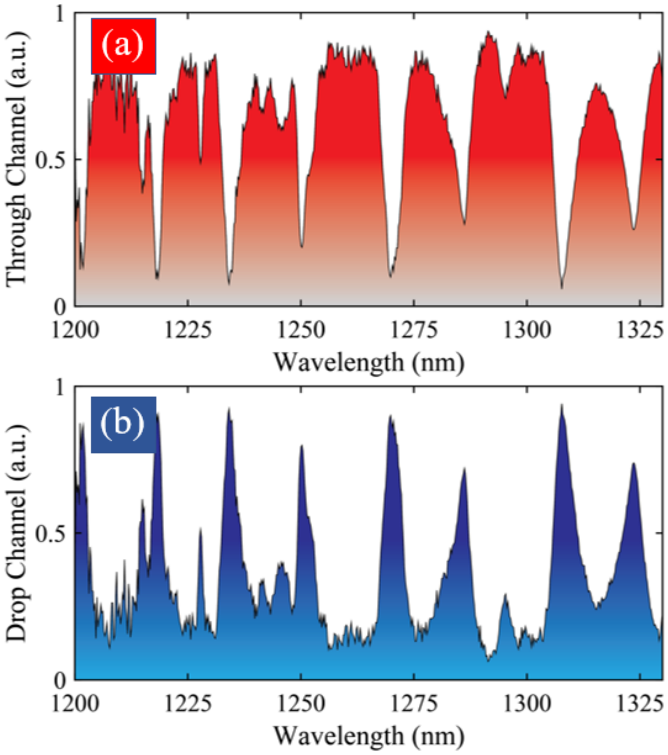

Figure 19. Measured normalized intensity at the (a) through and (b) drop channels when exciting the ensemble of the quantum dots above their saturation power.

We observe multiple dips (peaks) in the spectrum of the through (drop) channel that are separated by a free spectral range of ~ 16 nm. The suppression ratio of the filter varies among different free spectral range windows. We measured the highest suppression ratio to be 6.6 dB.

3.4 *Single quantum dot filtering and routing*

To isolate the single quantum dot emission, we lowered the excitation power to 5 μW which is below the dot saturation level. Figure 20a shows the photoluminescence spectrum when we excited the quantum dots and collected the signal directly from the nanobeam. We observed multiple quantum dot emission lines which is consistent with our laser spot size and the quantum dot density of $10\ \mu m^{-2}$. Next, we measured the photoluminescence spectrum from the drop channel while still exciting the quantum dots with the same power (Figure 20b).

We observed a significant suppression of the photoluminescence signal while a narrow wavelength range at around 1234 nm transferred to the drop channel. The quantum dot emission highlighted by the red shaded box (Figure 20) is on resonance with the microdisk resonator and therefore efficiently transferred to the drop channel while other emission lines were strongly suppressed. To further illustrate this fact, we overlap the cavity resonance with the quantum dot emission collected directly on top of the nanobeam as shown in Figure 21.

Using integrated intensity of this quantum dot emission in Figure 20a and 20b, and the simulated ratio between waveguide-coupled and out-of-plane emission, we estimate a total device efficiency of 4%.

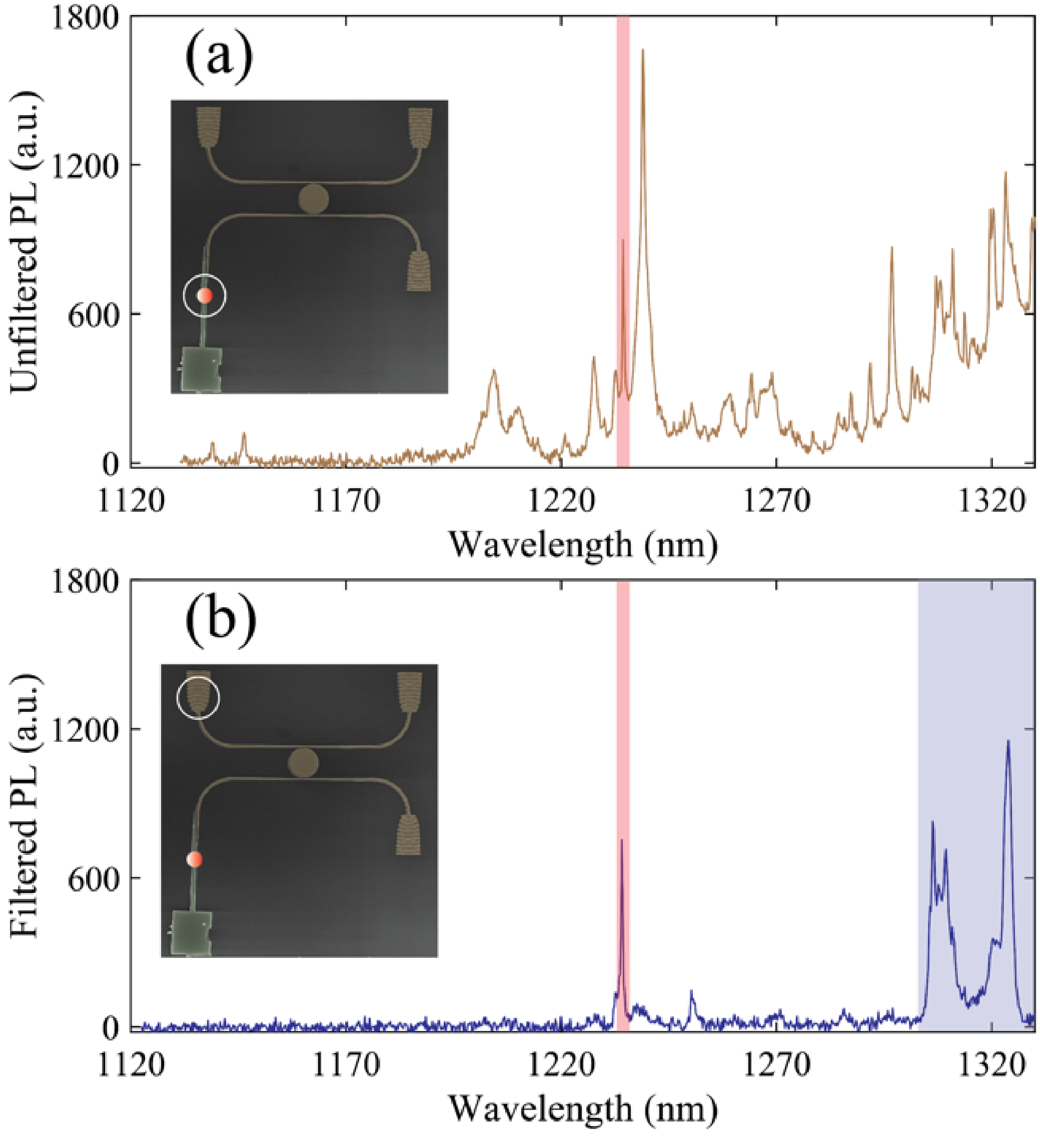

Figure 20. (a) Photoluminescence spectrum of the quantum dots when the excitation and collection spots are located on the nanobeam as shown in the inset. (b) Photoluminescence spectrum of the quantum dots when the excitation and collection spots are located on the nanobeam and drop channel, respectively. The shaded red boxes show the quantum dot emission that is transferred to the drop channel.

This value is smaller than the designed value of 29% and could be due to imperfect fabrication of the hybrid device, small misalignments between the nanobeam and the silicon waveguide, and imperfect position and orientation of the quantum dot with respect to the nanobeam. There is also a small signal observed at the drop channel around 1250 nm (Figure 20b), which may be a quantum dot emission coupled to another resonator mode. Moreover, multiple quantum dot emission lines couple to the resonator modes with wavelengths over 1300 nm (blue shaded box). The background suppression range can be expanded by designing resonators with a free spectral range larger than the inhomogeneous broadening of the quantum dots.

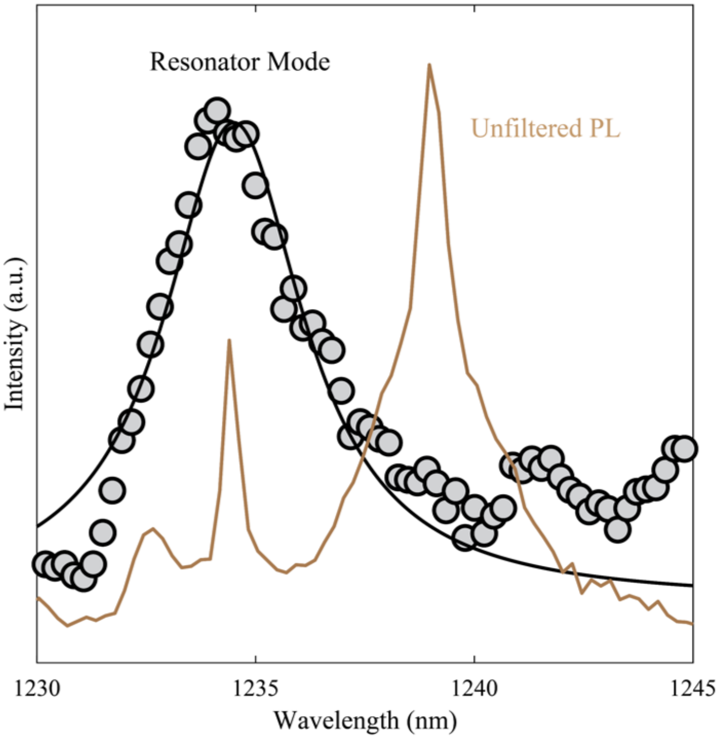

Figure 21. Spectrum of the unfiltered quantum dot emission measured on top of the nanobeam overlapped with the resonator mode. Black dots are the measured data and the solid curve is a Lorentzian fit to the data.

We also show that emission of a quantum dot can be routed to either the drop or through channels by tuning the dot wavelength with respect to the resonance of the microdisk. We use temperature tuning as a simple tool to tune the dot on and off resonance with the microdisk resonator. To be able to temperature-tune the emission wavelength of a quantum dot over the linewidth of the resonator we use one of the resonator modes (centered around 1364 nm) that has the highest quality factor (Q=661 obtained with a Lorentzian fit) and a quantum dot that is slightly blue-shifted from the resonator mode at 5 K. The shaded gray curve in Figure 22a shows a Lorentzian fit to the microdisk resonator response at the drop channel. The dashed vertical lines represent the emission wavelength of the quantum dot at different temperatures. By varying the temperature of the sample from 5 K to 50 K, we tune the emission wavelength over the entire resonance mode of the device. We note that we did not observe a shift in the resonance wavelength of the microdisk resonator in our measurements. This is because the refractive index of silicon is not very sensitive to temperature at cryogenic temperatures [64].

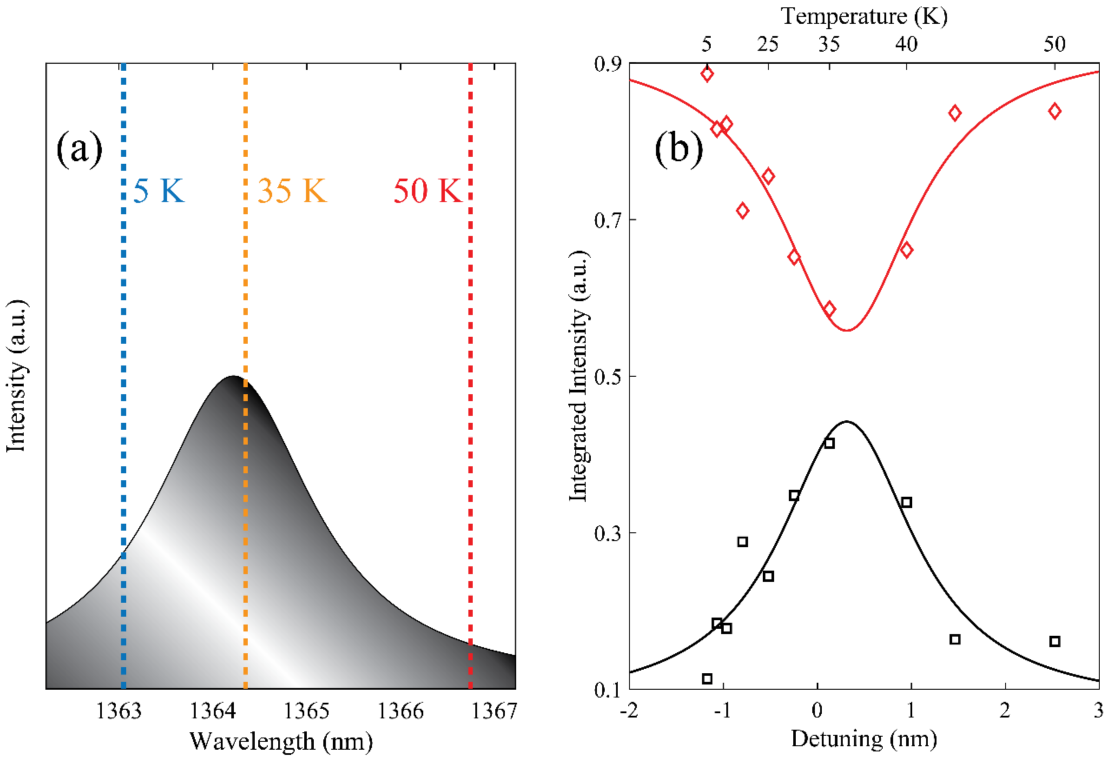

Figure 22. (a) A Lorentzian fit to the microdisk resonance (gray area) and center wavelength of the selected quantum dot at 5 K (blue), 35 K (orange), and 50 K (red). (b) The normalized integrated intensity of the dot for different detunings measured at the drop channel (black) and through channel (red). Top axis indicates the temperature at which the data was collected.

We collect the photoluminescence signal of the dot from both the through and drop channels at different temperatures. Figure 22b shows the normalized integrated intensity at different detunings (obtained at different temperatures) from the microdisk resonance for both the through and drop channels. We observe that when the dot is resonant with the resonator, it propagates to both the drop and through channels. However, when the emission wavelength is detuned from the resonance of the microdisk it mostly propagates to the through channel. We obtained a linewidth of 1.7 nm from Lorentzian fits to the integrated intensity of Figure 22b, which is consistent with the 2.06±0.4 nm linewidth from the gray curve in Figure 22a.

Ideally, all the emission should transfer to the drop channel at the resonance wavelength. However, fabrication imperfections in our silicon device prevents critical coupling between the waveguide and the resonator and leads to a small extinction ratio (i.e., the ratio between the maximum and minimum transmission) of 1.65.

3.5 Cavity tuning using laser heating

The temperature tuning approach described above, is a simple proof-of-principle demonstration that routing of the quantum dot emission is possible. However, increasing the temperature of the quantum dot can introduce dephasing mechanisms that could destroy the coherence of the quantum dot. A better approach would be either tuning the quantum dot with a less destructive mechanism such as quantum confined Stark effect or tuning the resonance of the cavity. We describe the former approach in chapter 5. In this section, we demonstrate a simple method for tuning the resonance of the cavity without any electrical contacts.

We shine a 650 nm continuous wave laser on the center of the disk which locally heats the device without increasing the temperature of the quantum dots (Figure 23a). By increasing the laser intensity up to 100 mW, we observe a red-shift of the cavity mode up more than 1 meV. Much more efficient switching of the cavity could be possible by introducing carefully designed electrodes [60] or using materials with electro-optic effect, an example of which will be described in chapter 4.

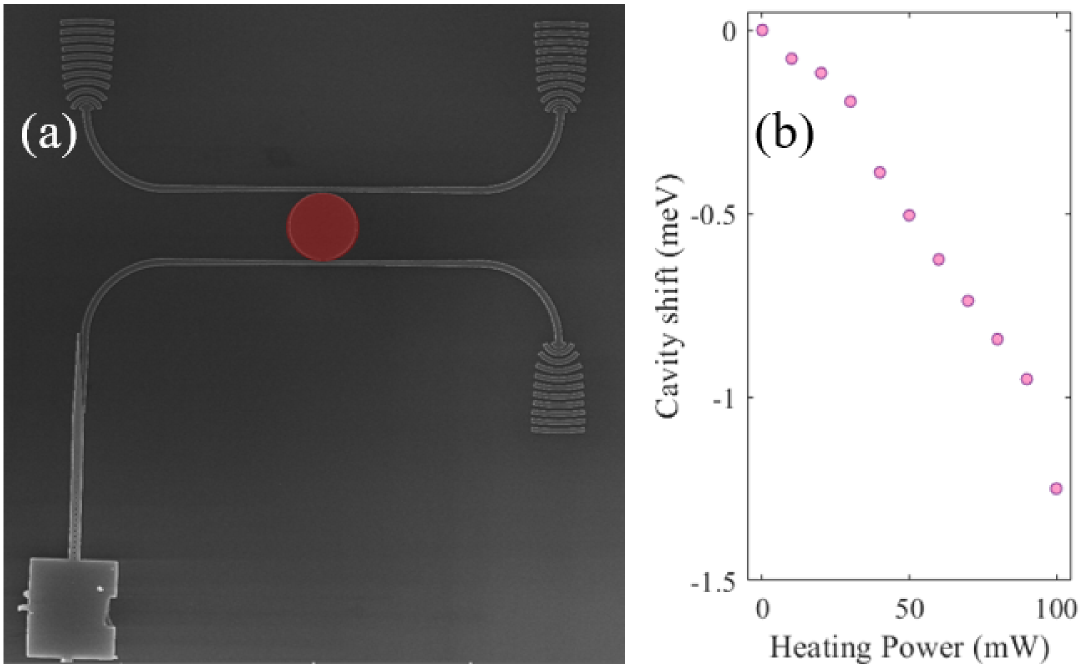

Figure 23. (a) Heating spot for tuning the cavity resonance (b) Observed cavity shift as a function of the laser power.

3.6 Summary and discussions

In summary, we have implemented a hybrid platform containing a silicon microdisk resonator and InAs quantum dots embedded in an InP nanobeam for filtering single quantum dot emission at telecom wavelengths. Using our integrated device, we achieved filtering of the background emission over a wide wavelength range while the desired quantum dot emission transfers through the filter. Moreover, by temperature-tuning a quantum dot over the resonance mode of the microdisk we controlled the transmission of the emission to the drop and through channels.

Improving the design of the filter for a higher free spectral range can enable suppression of the background over the entire range of the ensemble quantum dot emission. Furthermore, better design and fabrication accuracy is required to increase the extinction ratio of the routing. Replacing the disk resonator with a ring resonator may simplify the transmission spectrum by reducing the number of transverse modes. Incorporating electrical contacts for electro-optic switching of the router can achieve GHz modulation of the single photons. With improved extinction ratios and ultrafast switching available in silicon photonics, this platform may find applications in single-photon de-multiplexing [65], realizing linear optical quantum computing [29,66], and boson sampling [67].

Chapter 4: Integration of quantum dots with lithium niobate photonics

4.1 Introduction

Thin-film lithium niobate ($LiNbO_3$) is an emerging material platform for integrated photonics [13,68,69] that exhibits tightly confined optical modes, high refractive index, and wide transmission window (350 nm to 5 micron). Moreover, this material inherits the strong χ^2 electro-optic nonlinearity from $LiNbO_3$ bulk crystals [70–72], which enables ultrafast optical modulation. The tight confinement of the optical modes in thin-film $LiNbO_3$ significantly reduces the device size and facilitates scalable fabrication of many optical elements on a small chip. This scalability was not possible using conventional metal diffused waveguides, as they have large and loosely confined optical modes [73]. Recently, researchers have realized nanophotonic structures based on thin-film $LiNbO_3$ with low loss [74–77] and high modulation bandwidth[78] competing with the metal diffusion technology, but with a much smaller footprint, turning thin-film $LiNbO_3$ into a versatile platform for integrated photonic circuits.

Strong electro-optic non-linearity and compact nature of thin-film $LiNbO_3$ make it an ideal platform for quantum photonic circuits that can enable optical quantum computation [1,46,66,79–81], high-speed quantum communications [2,47], and simulation of non-classical problems in quantum physics [82], chemistry [45], and biology [83]. Many of these applications require quantum emitters that serve as both high-purity sources of indistinguishable single photons [3,4], and strong optical nonlinearities at the single photon level [84,85]. As a result, developing techniques for the integration of $LiNbO_3$ photonics with quantum emitters is an effective strategy for implementing fast reconfigurable quantum circuits. But to date this integration has yet to be demonstrated. One of the difficulties is that conventional metal diffused $LiNbO_3$ waveguides exhibit a small index contrast and large mode volume, which leads to poor transfer efficiencies for emitters that are embedded or evanescently coupled. But thin-film $LiNbO_3$ exhibits a much tighter mode confinement that could potentially solve this problem, which provides a new opportunity for quantum emitter integration.

In this chapter, we demonstrate integration of quantum emitters with $LiNbO_3$ photonic devices. Similar to chapters 2 and 3, the quantum emitters are InAs quantum dots embedded in an InP nanobeam, which serve as efficient sources of single photons in the telecom band [11,30]. We develop a hybrid device structure that efficiently transfers the emission from the dots to a $LiNbO_3$ waveguide. Tight confinement of the thin-film $LiNbO_3$ waveguide enables large mode overlap between InP nanobeam and $LiNbO_3$ waveguide that allows evanescent coupling [51,86] with efficiency exceeding 34%. Realizing such mode overlap between a nanostructure containing quantum dots and metal diffused $LiNbO_3$ waveguides would require a more complicated mode engineering potentially with very long adiabatic tapering. To experimentally demonstrate this approach, we fabricate the hybrid structure using the pick-and-place technique described in 1.6. We verify efficient transfer of emission from the quantum dot to the $LiNbO_3$ and confirm the single-photon nature of the emission with photon correlation measurements. This approach could enable scalable integration of single-photon emitters with complex $LiNbO_3$ photonic circuits that can rapidly modulate the photons and perform user-defined linear optical transformations on them.

4.2 Design considerations

Figure 24 shows the general scheme for coupling single-photon emitters with a $LiNbO_3$ waveguide. Figure 24a shows a cross-sectional illustration of the device which is composed of an InP nanobeam (500 nm wide and 280 nm thick) containing InAs quantum dots (with a density of ~10 μm^{-2}) on top of a $LiNbO_3$ waveguide. In the design we use a partially etched $LiNbO_3$ waveguides with 1200 nm width, which ensures the single mode condition at the InAs quantum dot wavelength of ~1300 nm while maintaining a relatively large top surface area to transfer the InP nanobeams. We note that unlike the vertical waveguides in silicon-on-insulator platform demonstrated in chapters 2 and 3, thin-film lithium niobate waveguides have a sidewall angle of around 30 degrees which is a direct consequence of its etching environment [87]. The lithium niobate waveguides in this chapter were fabricated by our collaborators at Harvard University.

The single photon from the quantum dot couples to the InP nanobeam and then smoothly transfers to the LiNbO3 waveguide through a 5 μm adiabatic taper (Figure 24b). A Bragg reflector at one end of the nanobeam, composed of a periodic array of holes with a period of 290 nm and radii of 100 nm, ensures the quantum dot emission propagates in only one direction.

We perform FDTD (Lumerical) simulations to estimate the efficiency of single photon coupling from the quantum dots to the InP nanobeam and subsequently to the $LiNbO_3$ waveguide. In our simulation, we model the quantum dots as electric dipole emitters with an in-plane polarization that are located at the center of the nanobeam. Figure 25 (a-c) display cross sectional views of light propagation in the hybrid device for different lengths of the taper. The simulation shows that emission from the quantum dot couples to the single mode of the InP nanobeam, and then adiabatically transfers to the $LiNbO_3$ waveguide as the taper narrows down. We calculate the coupling efficiency between the InP nanobeam and $LiNbO_3$ waveguide modes for a taper length of 5 µm to be 40.1%. A longer adiabatic taper can further improve this efficiency (See Figure 25d). However, for our current devices, we use a 5 µm taper length to make it easier to transfer the nanobeam onto the waveguide using the pick-and-place. The total efficiency from the quantum dot to the $LiNbO_3$ waveguide mode was calculated to be 34% by multiplying the efficiency of coupling for the quantum dot to the InP mode (85%) and the efficiency of InP to $LiNbO_3$ coupling (40.1%).

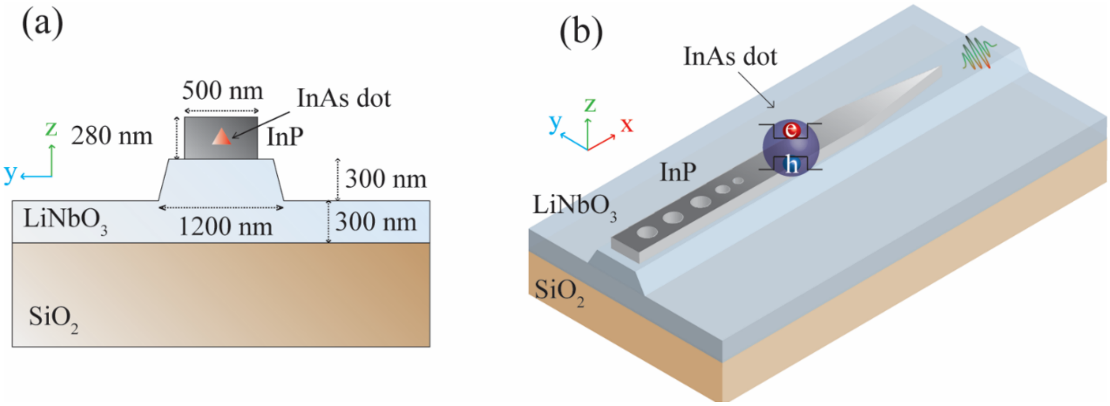

Figure 24. An illustration of the hybrid platform consisting of the $LiNbO_3$ waveguide and the InAs quantum dot embedded in InP nanobeam. (b) A side schematic of the hybrid device, showing the Bragg reflector on one side of the InP nanobeam and the adiabatic taper on the other side.

4.3 Lithium niobate waveguides

The substrate for the $LiNbO_3$ waveguides was a 600 nm thick X-cut $LiNbO_3$ film on 2 µm thick silicon dioxide (SiO_2) on a silicon substrate (obtained from NanoLN). We pattern the photonic structures with electron beam lithography using a hydrogen silsesquioxane (HSQ) resist. Next, we transfer the patterns onto a $LiNbO_3$ thin film using an optimized (Argon) Ar+ plasma etching recipe in a reactive ion etching tool.

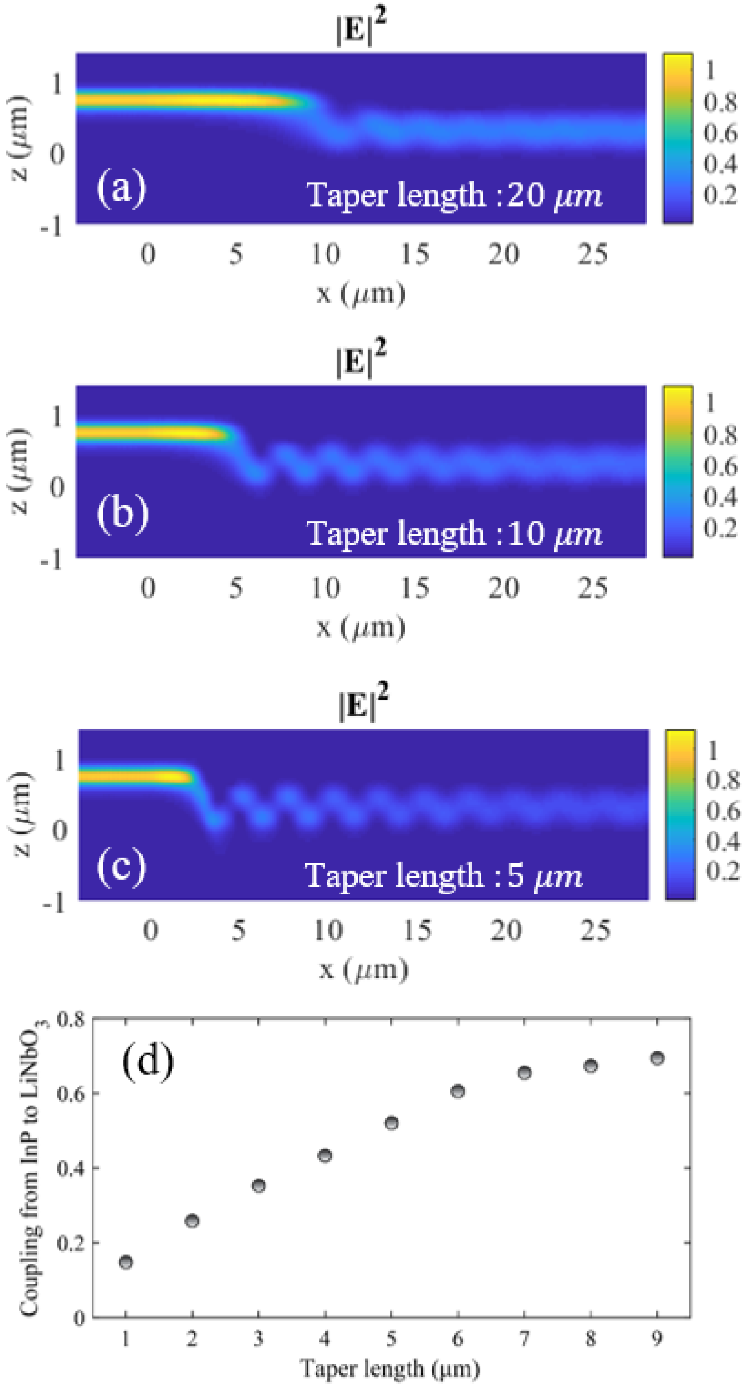

Figure 25. FDTD simulation of the electric field intensity $|E|^2$ in the coupling area for a taper length of (a) 20 μm, (b) 10 μm, (c) 5 μm. (d) Coupling efficiency from the nanobeam to the lithium niobate waveguide as a function of the taper length.

Finally, we remove the residual mask by buffered oxide etching. Figure 26 shows the fabricated waveguide structures as well as y-branch 50-50 beamsplitters. We terminated the waveguides with a periodic grating coupler with a period of 700 nm at one end of the structure for outcoupling the single-photon emission, with a calculated efficiency of 26.7%.

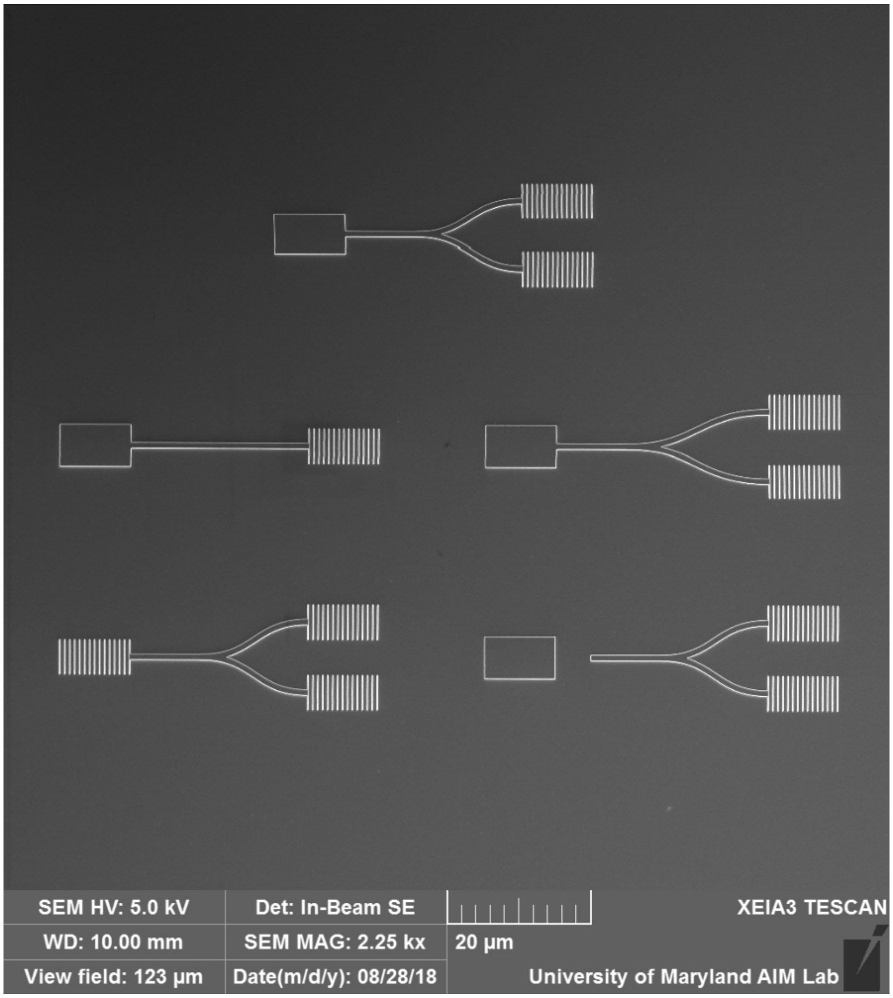

Figure 26. SEM image of the $LiNO_3$ straight waveguides and y-branch beamsplitters. The rectangular pads on the left end of the $LiNbO_3$ waveguides assist in the transfer process. Periodic grating couplers on the right side of the devices extract the light from the waveguides to the out-of-plane dimension.

4.4 *Hybrid integrated nanobeams on lithium niobate waveguides*

To form the InP nanobeams we follow the procedure in 1.7 and perform the pick-and-place using the method described in 1.6. Figure 27 shows SEM images of two integrated devices, one with a nanobeam on top of a $LiNbO_3$ waveguide (Figure 27a) and the other on top of a $LiNbO_3$ y-splitter (Figure 27b).

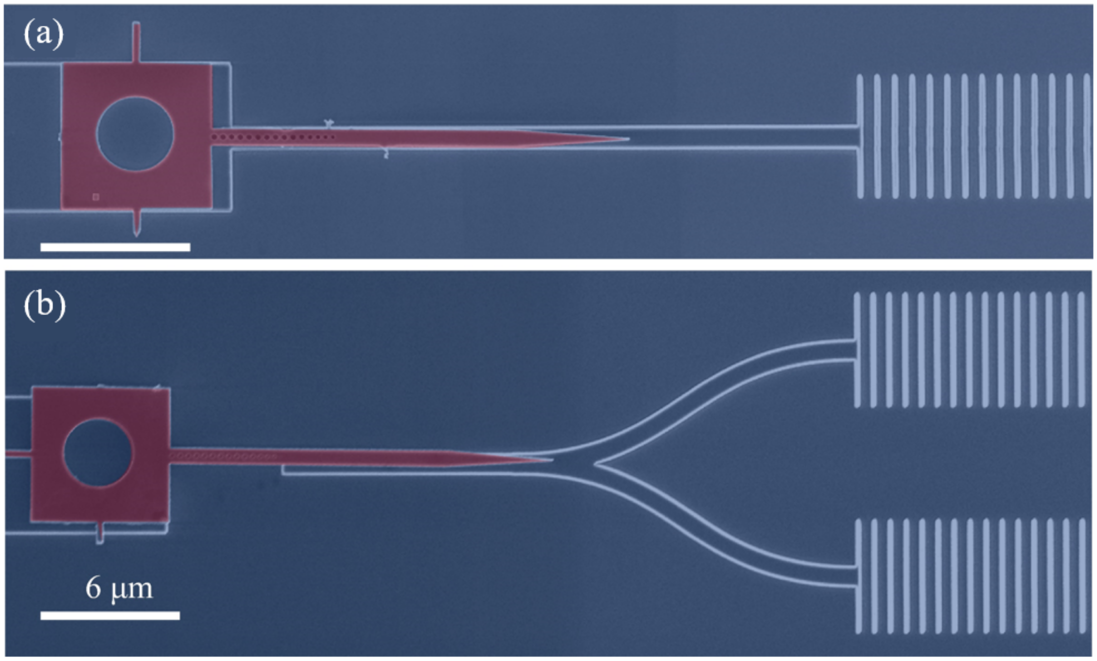

Figure 27. False color SEM image of the integrated InP nanobeam with a (a) straight $LiNbO_3$ waveguide and (b) an on-chip $LiNbO_3$ beamsplitter. Red and blue colors indicate InP and $LiNbO_3$, respectively. Scale bar is 6 μm for both panels.

Using the setup described in 1.8, we excite the quantum dots with a 780 nm continuous wave laser and collected the photoluminescence spectrum through the grating couplers. Figure 28a shows the photoluminescence spectrum taken from the straight $LiNbO_3$ waveguide integrated with quantum dots. We observe multiple emission lines in the photoluminescence spectrum that confirms the coupling of multiple spectrally resolved quantum dots.

To assess the photon collection efficiency in our hybrid device, we use a 785 nm pulsed laser excitation with 40 Mhz repetition rate. Correcting for our setup efficiency, we calculated a collection efficiency of 2.2% at the first lens for a representative coupled quantum dot labeled as QD1 in Figure 28a. This value is lower than the ideal collection efficiency of 9% that we determined from our simulations. The simulated collection efficiency is the product of the coupling efficiency from the quantum dot to $LiNbO_3$ (34%) and the grating coupler efficiency (26.7%). We attribute the lower experimental collection efficiency to small fabrication imperfections, residual misalignment of the nanobeam with the $LiNbO_3$ waveguide, and quantum dot deviations from the center of the nanobeam as carefully discussed in chapter 2. Figure 28b shows the time-resolved photoluminescence signal from QD1. We fit the time-resolved data to a single exponential decay model and obtain an excited state lifetime of $\tau = 1.77 \pm 0.03\, ns$.

To confirm the single photon nature of the emission, we perform second order photon correlation measurements on several of the coupled quantum dot emission lines. We send the collected signal through the grating coupler to a fiber beamsplitter and connected the two output ports of the beamsplitter to different single-photon detectors. Figure 29a shows a continuous wave second-order correlation measurement for QD1, using a 780 nm laser. The measurement shows a clear antibunching behavior. We fit the antibunching dip to a function of the form $g^{(2)}(\tau)$= 1- (1- $g^{(2)}(0)$) exp(-$|\tau|/\tau_0$) without dark count subtraction or deconvolution and obtained $g^{(2)}(0) = 0.08$. Moreover, we perform pulsed photon correlation measurement (as shown in Figure 29b), and observe an antibunching behavior with $g^{(2)}(0) = 0.25$. Both of these values are lower than the classical limit of 0.5. Background emissions due to our non-resonant excitation cause the residual multiphoton events resulting in non-ideal $g^{(2)}(0)$ values in our photon correlation measurements. As mentioned previously in 2.5, these measurements could benefit from resonant excitation [34,88] or quasi-resonant excitation [35,89] which significantly reduce the background emission.

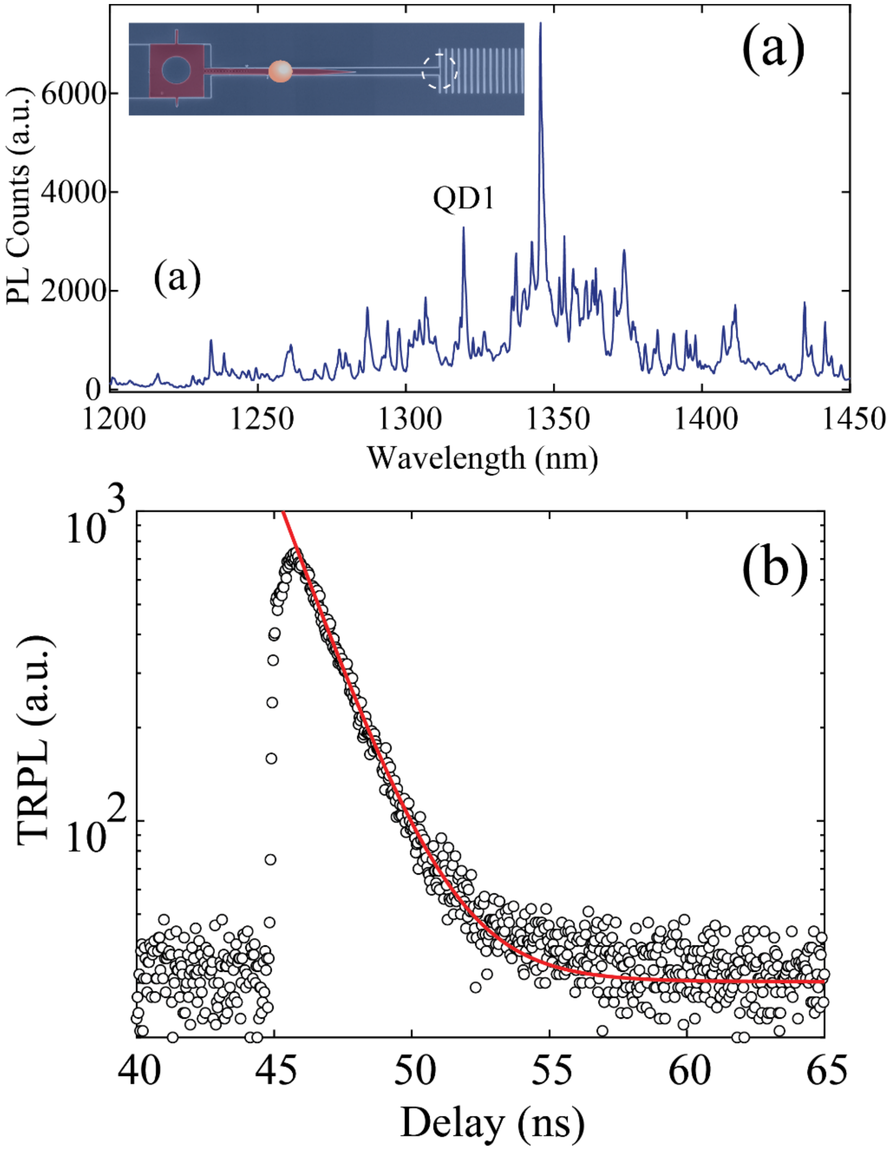

Figure 28. (a) Photoluminescence spectrum of the waveguide coupled quantum dots when we excite the quantum dots on top of the nanobeam and collect the signal through the grating. (b) Time-resolved photoluminescence signal from the QD1 labeled in (a). The red curve is a single exponential fit to the data.

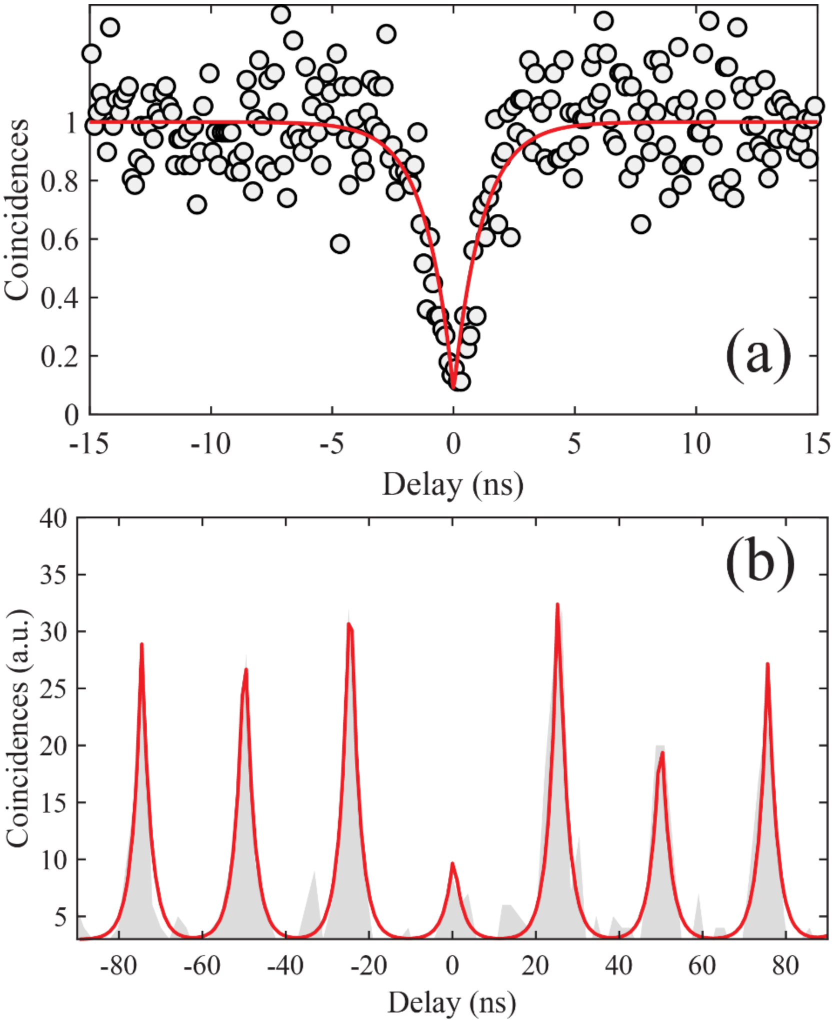

Figure 29. Second order photon correlation measurement of QD1 when excited with (a) continuous wave laser and (b) a pulsed laser. The curves in both panels are exponential fits to the data.

4.5 Lithium niobate on-chip beamsplitter

In this section, we investigate the hybrid device in Figure 27b that integrates quantum dots in the InP nanobeam with an on-chip $LiNbO_3$ beamsplitter. We excite the quantum dots directly from the top of the nanobeam and collected the photoluminescence signal from both grating couplers. We separate the signal from each grating using a pick-off mirror in free space and sent each port to separate spectrometers that acted as spectral filters. Figure 30a and 30b show the collected photoluminescence signal from the top and bottom gratings. We observed multiple quantum dot lines in both spectra. We identified 7 emission lines that appear in both spectra, suggesting that they originate from the same quantum dots.

To confirm that the replicated emission lines in Figure 30 originate from the same quantum dot, we performed a photon correlation measurement on the quantum dot represented by line 4, and spectrally filter out all other emission lines. Figure 30c shows the second-order photon correlation measurement of this emission using continuous wave excitation, with $g^{(2)}(0) = 0.36$. The measured $g^{(2)}(0)$ value is degraded as compared to the measurement in Figure 29. This degradation is due to the fact that the device with on-chip beamsplitter exhibited a poorer coupling efficiency, which required higher excitation power in order to obtain a second-order correlation. This higher excitation drove the quantum dot closer to the saturation level, resulting in a higher background level. This measurement demonstrates that the two matched lines from the grating couplers originate from the same quantum dot. The on-chip $LiNbO_3$ beamsplitter enables the direct measurement of a second-order photon correlation from the quantum dots coupled to the $LiNbO_3$ waveguide without an external beamsplitter. Implementing this functionality on-chip is a step toward scalable integration of multiple single-photon emitters with more complex $LiNbO_3$ photonic circuits, where most of the light manipulations happen on a compact photonic chip.

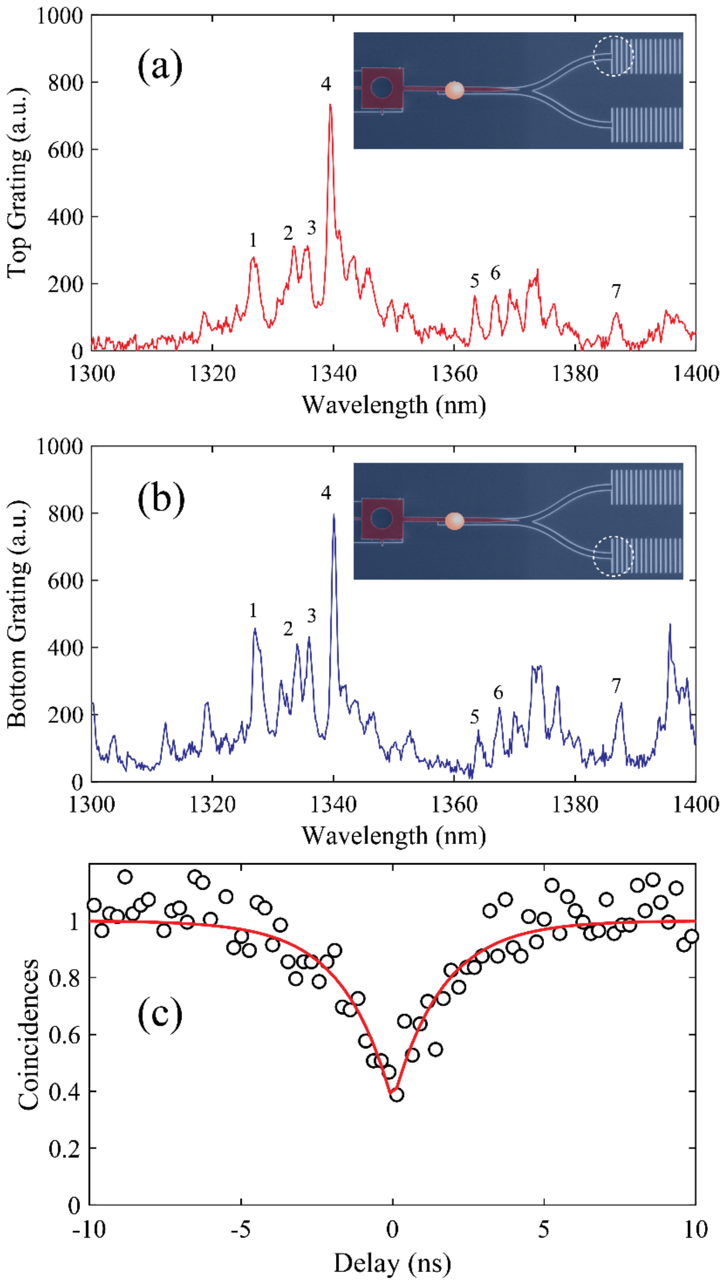

Figure 30. (a,b) Photoluminescence spectrum collected through the (a) top and (b) bottom gratings. (c) Second order correlation measurement of emission line 4, labeled in (a,b).

4.6 Summary and discussions

In summary, we have deterministically coupled quantum emitters to a nanophotonic $LiNbO_3$ waveguide. We confirmed the coupling of single photons to straight waveguides and y-branch beamsplitters using photon correlation measurements. The collection efficiency of our devices was limited by the performance of the grating couplers. More efficient grating coupler design or better approaches of light collection, such as edge coupling [37], tapered fibers [38], or the incorporation of detectors on the chip [90], could boost the collection efficiency. Incorporation of Mach-Zehnder or resonator based electro-optic switches [78] would allow fast switching of single photons. Moreover, by pre-characterizing the quantum dot devices before pick-and-place [91], we can overcome the spectral and spatial randomness of the quantum dots and select the devices with emitters at the same resonance wavelength.

In this way, we can efficiently extend our results to complex $LiNbO_3$ circuits containing many identical single-photon emitters. Results demonstrated in this chapter, represent an important step toward routing and fast feedforwarding of on-demand single photons on a chip, which could enable high speed quantum communication [2,47] and linear optical approaches for photonic quantum computing [1,80].

Chapter 5: Large Stark tuning of InAs/InP quantum dots

5.1 Introduction

As discussed in previous chapters, epitaxial InAs quantum dots embedded in InP (InAs/InP) are excellent sources of telecom single photons [31,92]. Previous studies have demonstrated single-photon generation in these materials with large Purcell enhancement [93] and record high single-photon purity [30]. InAs/InP quantum dots can also act as indistinguishable single-photon sources at telecom wavelengths suitable for quantum communications [11]. Many applications in quantum information processing require multiple identical quantum emitters. However, the emission wavelength of individual quantum dots varies due to small differences in their shape, size, strain environment, and chemical composition. This makes it difficult to integrate multiple identical quantum emitters on the same chip. To overcome this spectral randomness, we need a method to tune the emission wavelength of individual dots over a broad spectral range without degrading the coherence properties of the emitter.

Stark tuning is an effective technique to tune the wavelengths of quantum dots. This technique uses an electric field to tune the emission wavelength using the quantum-confined Stark effect. In InAs/GaAs quantum dots emitting at wavelengths below 1 μm, Stark tuning has produced wavelength shifts of up to 25 meV with minimal degradation of emission properties [94,95], enabling two different dots to show two-photon interference [49,96]. Large Stark tuning at telecom wavelengths has been demonstrated in InAs quantum dots embedded in GaAs [97] or InAlGaAs [98]. However, the extension of this approach to InAs/InP has not been studied carefully.

Previous Stark tuning demonstrations of InAs/InP quantum dots suffered from a limited tuning range of < 0.8 meV [99,100], because at high electric field intensities the dot gains additional charges that cause discrete jumps in the optical spectrum. Achieving large wavelength tuning ranges requires new device geometries that limit this charging effect.

In this chapter, we demonstrate a large DC Stark shift in the emission wavelength of InAs/InP quantum dots at telecommunication wavelengths. We place the InAs quantum dots embedded in InP between two metallic plates that are separated by a SiO_2 buffer layer to avoid introduction of charges. An applied DC electric voltage shifts the emission of the quantum dot by more than 5 meV without any observed spectral jumps due to charging, providing a much larger tuning range than previously available for this material. Steady-state and time-resolved photoluminescence measurements show a clear tunneling effect introducing non-radiative decay processes that limit the emitter brightness at high voltages. Photon correlation measurements show robust anti-bunching behavior over a wide voltage range. We also examine a lateral electric field geometry which leads to a significantly less efficient tuning range.

Our results pave the way for developing large identical arrays of quantum emitters at telecom wavelengths. Such identical quantum emitters are highly desirable for quantum information applications, such as boson sampling [67], quantum communication [2], and optical quantum computing [1,46,81]. Furthermore, our technique is agnostic to the nature of the substrate, and could thus be incorporated in more complex hybrid photonic device structures that combine quantum dots with silicon photonics [20] or lithium niobate photonics [23].

5.2 Vertical field device

Figure 31a shows the proposed device, in which the InAs/InP quantum dots are located between two metal plates that provide the vertical DC electric field for Stark tuning. We pattern the bottom contact on a silicon carrier chip with electron beam lithography followed by metal deposition (5 nm Chromium (Cr)/50 nm Gold (Au)) and lift-off. Next, we use a microprobe to transfer an InP waveguide containing InAs quantum dots onto the bottom contact as described in 1.6 and cover the sample with 500 nm SiO_2 deposited by plasma enhanced chemical vapor deposition. Then we form the top contact by electron beam lithography, followed by 20 nm Cr deposition and lift-off. We chose a thin Cr layer to have optical access through the contact. Finally, we open a window in the SiO_2 by buffer oxide etching to electrically access the buried metal pad connected to the bottom contact. Figure 31b shows a false color SEM image of the fabricated device.

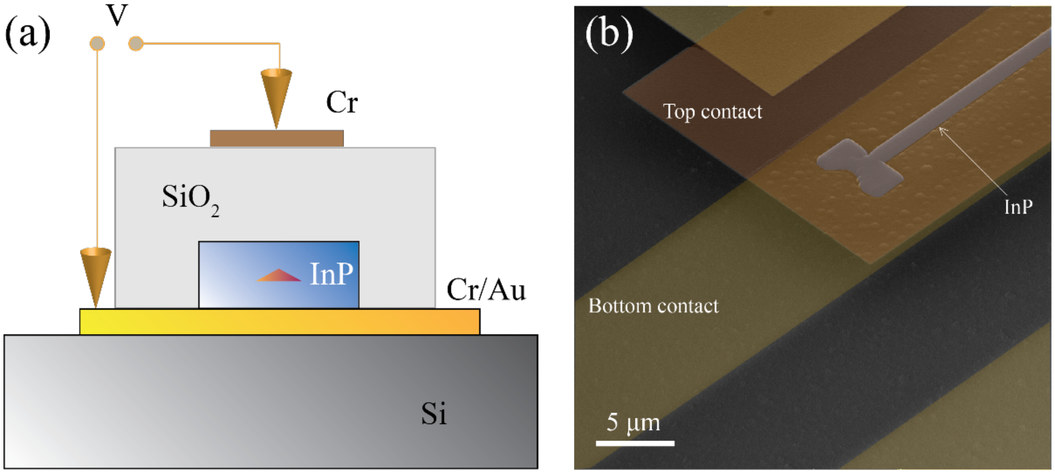

Figure 31. (a) An illustration of the proposed Stark tuning device structure. (b) False color SEM image of the fabricated sample.

Figure 32 shows the photoluminescence spectrum of multiple quantum dot emission lines at different DC electric voltages using the measurement setup described in 1.8. All quantum dot emission lines start to red shift as we introduce the voltage due to the quantum confined Stark effect.

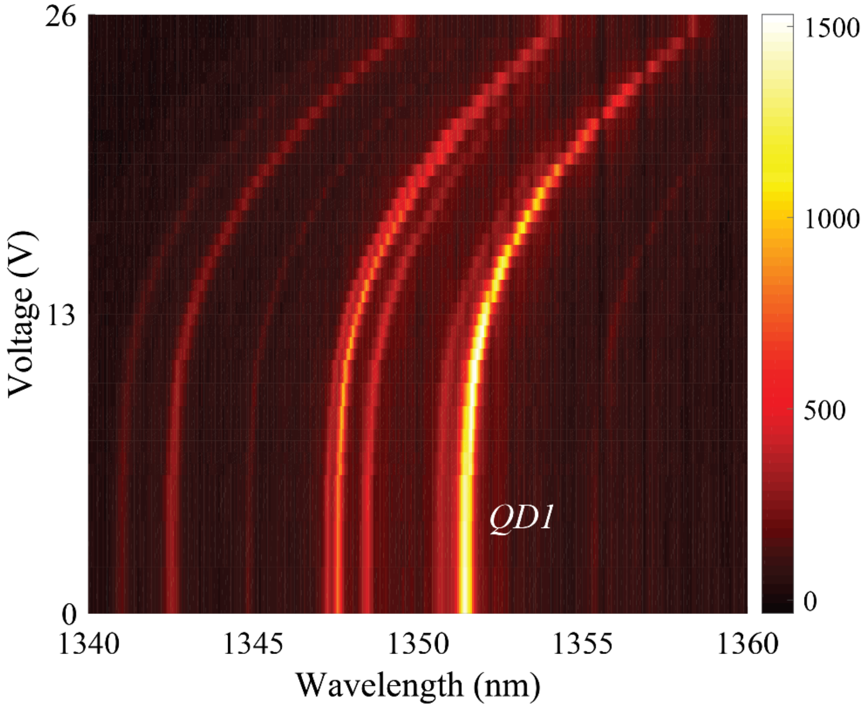

Figure 32. Photoluminescence spectra of several quantum dots for different gate voltages.

We extracted photoluminescence emission properties (center wavelength, integrated intensity, and linewidth) from Lorentzian fits to the photoluminescence spectrum at each applied voltage. The relative change in the center wavelength of a quantum dot (QD1) that we labeled in Figure 32 is shown in Figure 33a. We observe a large shift in the emission wavelength of up to 8 nm (5.1 meV) and attribute it to the quantum confined Stark effect. A quadratic fit of the form $\Delta E = pF + \beta\, F^2$ to this shift allows us to determine the polarizability (β) and dipole moment (p) of the InAs/InP quantum dots. Here ΔE is the relative change in emission energy and F is the electric field intensity. In order to obtain F from the applied voltage, we perform electrostatic

COMSOL simulation for our device geometry that considers the dielectric constant of all the materials as well as the curvature due to oxide deposition as shown in Figure 34.

From the fit we obtain $\beta = 0.19 \pm 0.01\ \mu\text{eV}\frac{\text{cm}^2}{\text{kV}^2}$ and $p/e = 0.14 \pm 0.02$ nm, where e is the charge of an electron. These values are slightly lower than the previously reported values for InAs/InP quantum dots [99,100]. Different growth conditions and shape of the quantum dots, parasitic resistance in the device [101], and non-ideal thickness of the insulator could explain the lower measured values of dipole moment and polarizability compared to the previous works.

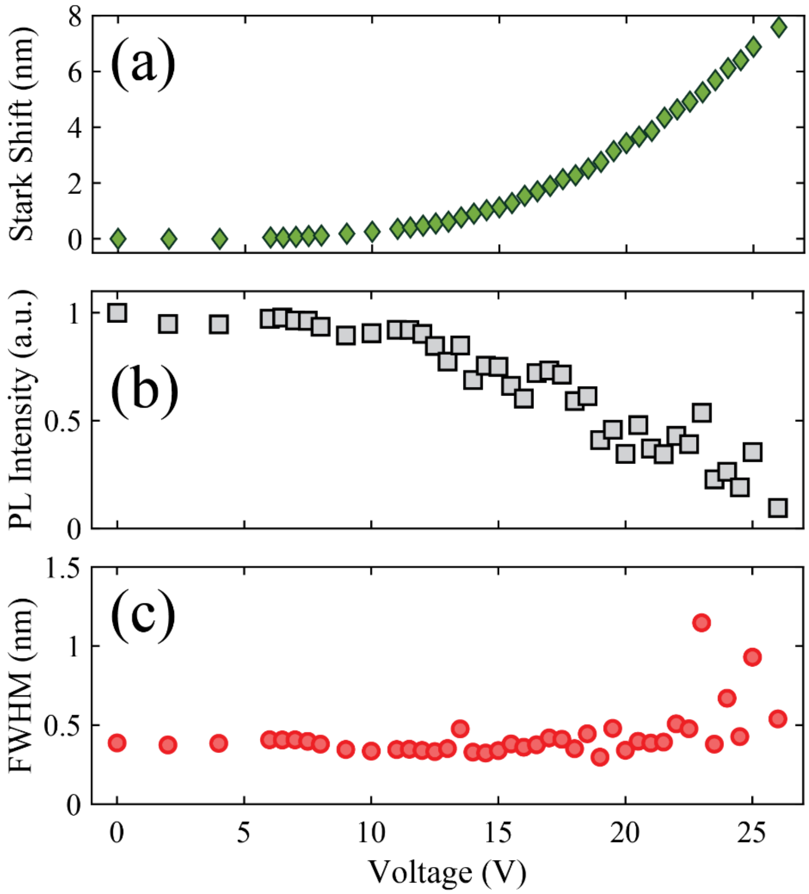

Figure 33. (a) The Stark shift of QD1, (b) normalized intensity of QD1, and (c) full width at half maximum for QD1 when fitted to a Lorentzian function, all as a function of applied DC voltage.

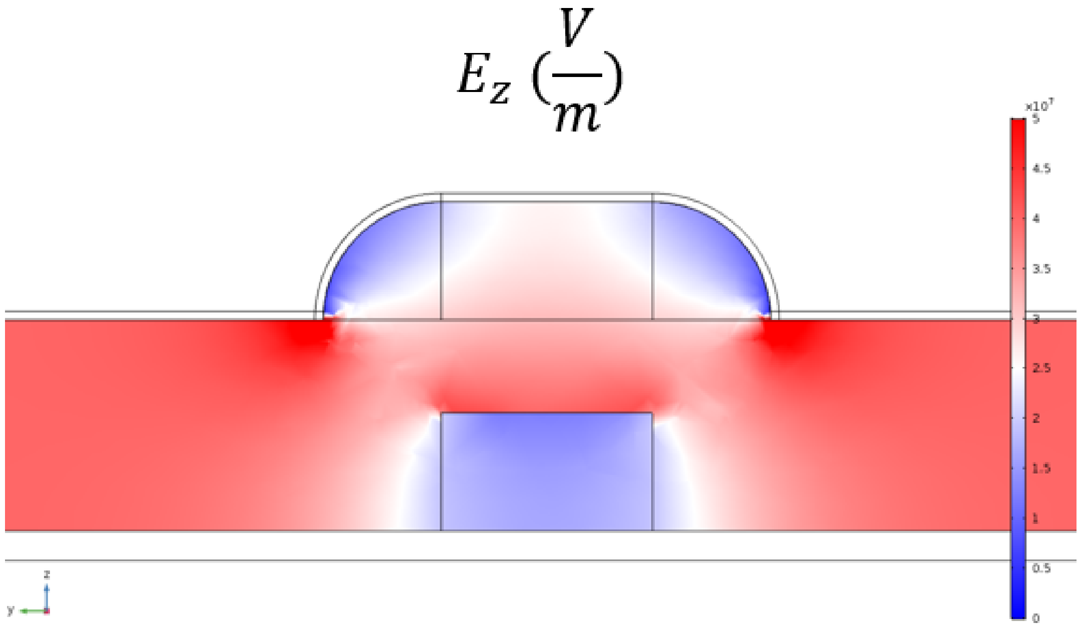

Figure 34. Electrostatic COMSOL simulation of the vertical electric field for an applied voltage of 20 V, which leads to $E_z = 1.55 \times 10^7 V/m$ at the center of the waveguide.

Figure 33b and 33c show the integrated intensity and linewidth of the QD1 emission as a function of the applied voltage. The integrated intensity of the QD1 emission at 26 V drops to ~10% of its initial value at 0 V applied voltage. At large electric field intensities (See Figure 35) the created carriers are no longer confined in the quantum dot potential, which leads to tunneling [102,103]. Carrier tunneling reduces the efficiency of emission and therefore explains the drop in integrated intensity.

The linewidth of QD1 (Figure 33c) remains constant until very high electric field intensities. We observe linewidth variations among different quantum dots. The particular dot (QD1) we studied has a broad linewidth, but other quantum dots in the sample can feature much narrower linewidths and can exhibit two-photon interference [42,104]. Therefore, narrow linewidth quantum dots combined with our Stark tuning approach are promising for multi-photon interference applications.

Before moving on to time-resolved and photon correlation measurements, we note that the large tuning demonstrated in QD1 was not a rare occasion on our chip. We also measured shifts of similar size for 9 different quantum dots on the same chip as demonstrated in the histogram plot in Figure 36.

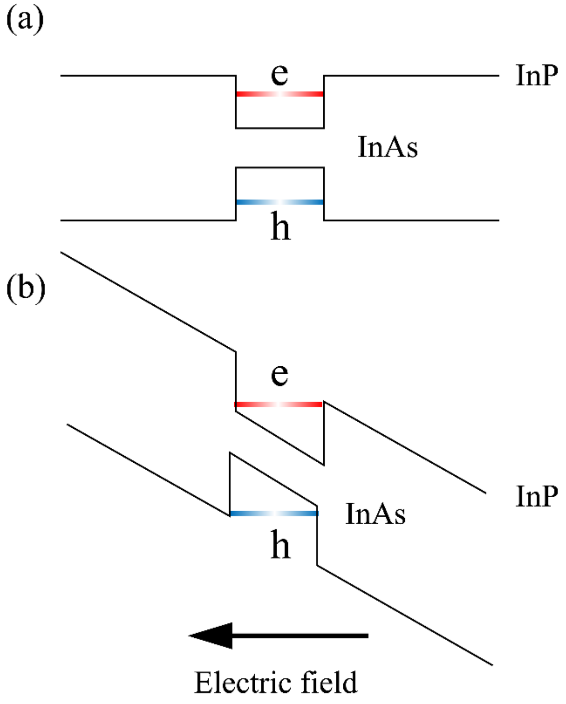

Figure 35. Schematic band diagram of a single InAs/InP quantum dot (a) without and (b) with an applied electric field.

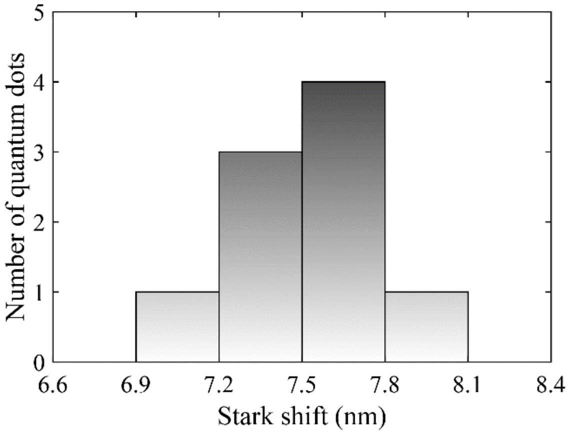

Figure 36. Histogram plot of Stark shift measured from 9 different quantum dots on the same chip at 26 V.

5.3 Time-resolved photoluminescence measurement

The carrier tunneling effect also represents itself in the excited state lifetime of the quantum dots. Time-resolved photoluminescence measurements reveal changes in the lifetime due to oscillator strength modification as well as tunneling effects [95]. To measure the lifetime of the quantum dot emission, we used a 785 nm pulsed laser with 40 MHz repetition rate. Figure 37 shows the evolution of the lifetime as we changed the applied voltage. Initially, at 0 V the lifetime is 1.44 ns and at higher electric fields (V = 28 V) the lifetime increases to 1.71 ns. We attribute the longer lifetime to the decrease in the oscillator strength of the quantum dot caused by larger separation of the electron-hole pair [105]. At even larger electric field intensities, tunneling effects dominate the lifetime and reduce it to 1.39 ns [95,105]. The rich dynamics of these two competing processes were absent in the photoluminescence intensity measurement (Figure 33b), because both the tunneling effect and oscillator strength reduction lead to a decrease in the emission intensity.

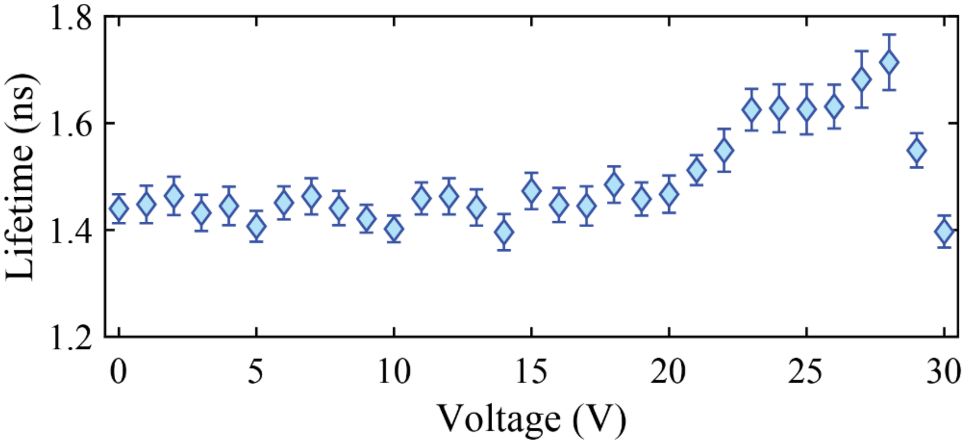

Figure 37. Excited state lifetime of QD1 labeled in Figure 32 as a function of the applied voltage.

5.4 Second-order photon correlation measurement

As mentioned in the previous chapters, single-photon emission from quantum dots is vital for their application in quantum information processing. Therefore, we perform photon correlation measurements at two different voltages to confirm the single-photon nature of the quantum dot emission and its stability while applying an electric field for Stark tuning. We use a 780 nm continuous-wave laser to excite the quantum dots and send the photoluminescence signal to a grating spectrometer to filter the emission from QD1. The filtered signal is then sent to a fiber-based beam splitter followed by two superconducting single-photon detectors.

Figure 38a and 38b show the second-order photon correlation measurements for QD1 at 0 V and 19 V, respectively. Both measurements show clear antibunching behavior, confirming the single photon emission from QD1 even when the emission wavelength was shifted by ~1.8 meV. From exponential fits to the raw data without any deconvolution or background subtraction we obtain $g^{(2)}(0) = 0.12 \pm 0.18$ and $g^{(2)}(0) = 0.31 \pm 0.18$ for applied voltages of 0 V and 19 V, respectively.

To determine the effect of the electric field on the single-photon purity of the emission, we measure the background (including the detector dark counts) for both voltages by disconnecting the quantum dot signal from one of the single photon detectors [11]. We subtract the background from the measured coincidences and fit the subtracted data to an exponential function without any deconvolution. From the fits, we obtain $g^{(2)}(0) = 0.02 \pm 0.2$ and $g^{(2)}(0) = 0.09 \pm 0.22$ for applied voltages of 0 V and 19 V, respectively. To the extent of our error bounds, the $g^{(2)}(0)$ at 19 V does not degrade from its original value at 0 V and remains below the classical limit of 0.5, indicating the robustness of single-photon emission against Stark tuning.

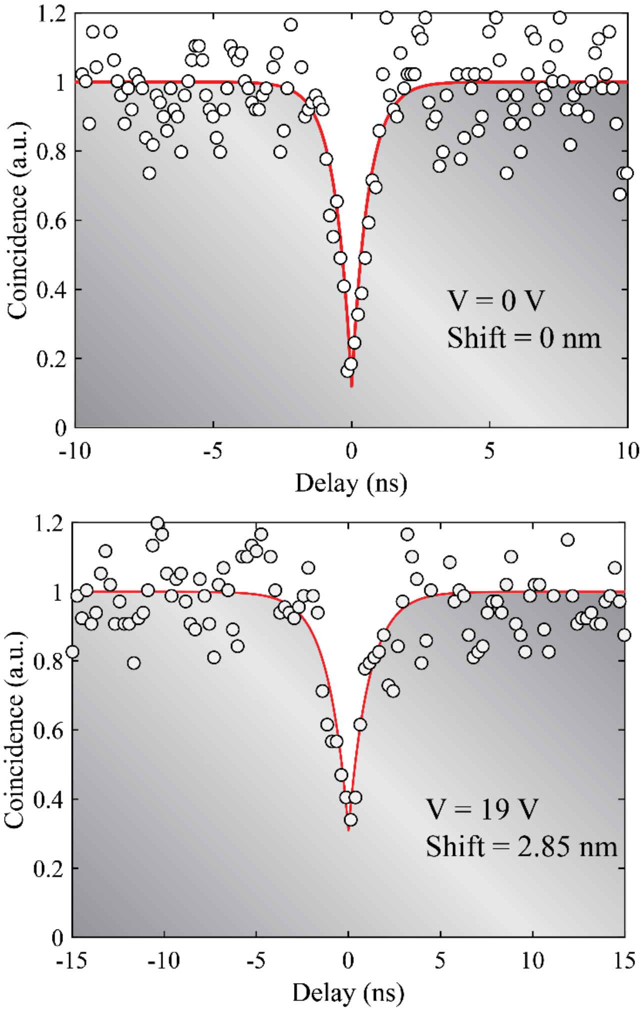

Figure 38. Second-order photon correlation measurement for QD1 at (a) 0 V and (b) 19 V.

5.5 Lateral field device

In addition to the device based on vertical electric field, we also fabricate devices that support lateral (i.e., in-plane) electric fields. Figure 39a shows a schematic of the device that contains two Cr/Au electrodes on each side of the InP waveguide embedded with quantum dots. To experimentally realize such a device, we first deposit the electrodes on a sapphire substrate and then using the pick-and-place approach introduced in 1.6, we transfer an InP waveguide to the gap between the two electrodes.

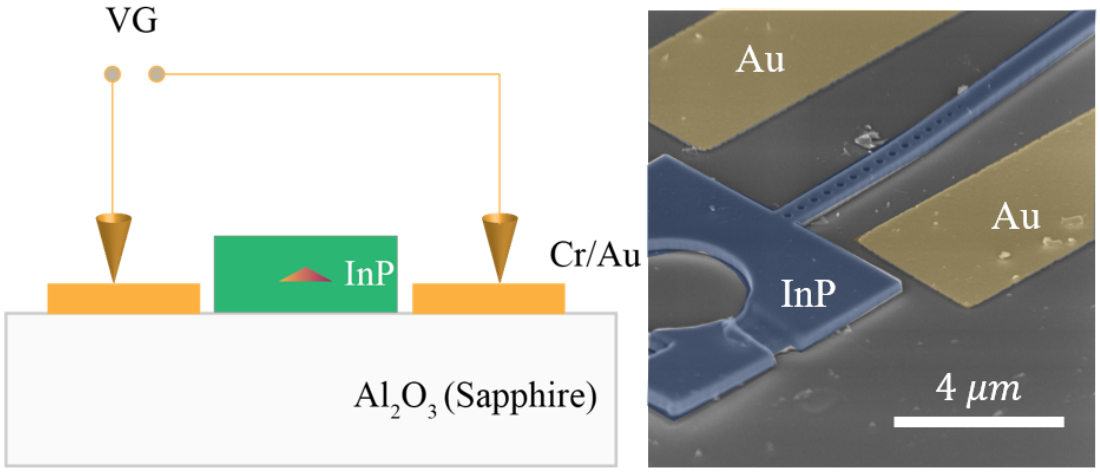

Figure 39. (a) A schematic of the proposed device with lateral electric field. (b) False color SEM image of the fabricated device. Blue and gold correspond to InP waveguide and deposited gold electrodes, respectively.

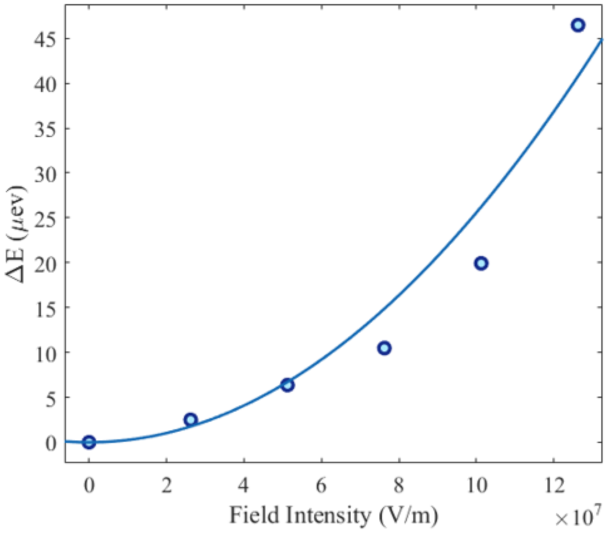

Figure 40. Change in the emission energy as a function of applied electric field intensity for a representative quantum dot.

Similar to 5.2, we perform photoluminescence measurements while varying the applied lateral voltage. Figure 40 shows the shift in the emission energy of a representative quantum dot as a function of electric field intensity. In this measurement, we raise the applied voltage up to $500\ V$, and only observe Stark shifts of $\sim 50\ \mu eV$, which is two orders of magnitude smaller than the shift observed in the vertical field device. The blue cure in Figure 40 is a quadratic fit of the form $\Delta E = pF + \beta\ F^2$. Due to small tuning capability, this device geometry would be less promising for compensating spectral differences in quantum dots. Therefore, we did not pursue the time-resolved and photon correlation measurements as we did for the vertical field device in 5.3 and 5.4.

5.6 <u>Summary and discussions</u>

In this chapter, we have demonstrated a large Stark shift in the InAs/InP quantum dot emission wavelength, which is promising for the realization of multiple identical telecom single-photon emitters on a chip. Photon correlation measurements demonstrate robust single-photon emission of the quantum dots before and after Stark tuning. Introduction of wide bandgap barrier layers during the quantum dot growth can reduce the carrier tunneling rates. Therefore, Stark tuning range will only be limited due to reduction in oscillator strength and should further increase [95]. Photon collection in this device is based on out-of-plane radiation of the quantum dot through the top metal contact. Using fully transparent top contacts, such as graphene [106] and indium tin oxide [107], can prevent photon reflection at the top contact and improve the photon collection efficiency. Furthermore, integrating these wavelength-tunable single-photon emitters with integrated photonic waveguides will enable an on-chip optical network with multiple identical quantum emitters for studying multi-photon interference effects [67], quantum simulation [45,82], and linear optical quantum computation [1,81].

Chapter 6: Optical amplification with a single quantum dot strongly coupled to a cavity

6.1 Introduction

One missing element in the quantum photonics toolbox to perform deterministic quantum information processing applications is photon-photon interactions. Naturally, photons do not interact with one another. An effective approach to overcome this limitation is to leverage the strong light-matter interaction in quantum emitters [108].

Nanophotonic cavities coupled to quantum emitters can enhance the rate of light-matter interactions by confining the light in a small mode volume. Photonic crystal cavities are particularly interesting because they offer high quality factors in small mode volumes, which are both beneficial for enhancing the interactions between the photons and the quantum dot [85].

In this chapter, we describe our preliminary results on amplification of weak optical signals using a strong pump laser that inverses the population of a quantum dot. Our system consists of a single InAs/GaAs quantum dot strongly coupled to a photonic crystal cavity. Moreover, the quantum dot is electrically controlled using a p-i-n diode structure that was formed during the MBE growth of the sample [109]. We observe that without the pump laser, our coupled system shows a familiar polaritonic behavior where the reflectivity is attenuated at the cavity resonance. However, increased pump power can inverse the quantum dot population which leads to a significantly different cavity reflectivity where the reflectivity is amplified at the resonance of the cavity. We attribute this amplification to stimulated emission from the quantum dot.

6.2 Device concept and fabrication

Figure 41a shows an illustration of our measurement scheme. A single InAs/GaAs quantum dot is located at the center of the photonic crystal cavity. A strong laser excites the quantum dot from its ground state $|g\rangle$ to one of the excited states $|e\rangle$, which rapidly decays to the excitonic state $|X\rangle$ (Inset of Figure 41a). Since the $|e\rangle \rightarrow |X\rangle$ transition is much faster than the $|X\rangle \rightarrow |g\rangle$ transition, a population inversion could occur using a continuous wave laser [110].

We also probe the cavity reflectivity using a weak laser that is resonant with the $|X\rangle \rightarrow |g\rangle$ transition. In the following sections, we compare the cavity reflectivity obtained from the probe signal for different powers of the pump laser. We note that the pump laser itself causes fluorescence from the quantum dot, which we subtract from the probe signal to obtain the reflectivity at each pump power.

To experimentally realize this system, we fabricate a photonic crystal cavity on the GaAs sample that contains quantum dots. The cavities are based on the design described in Akahane et al. [111]. To fabricate the suspended GaAs cavities, we follow a similar approach as in 1.7 with slight modifications. A complete description of the fabrication method is provided in Luo et al. [109]. Figure 41b shows a SEM image of the fabricated photonic crystal cavity.

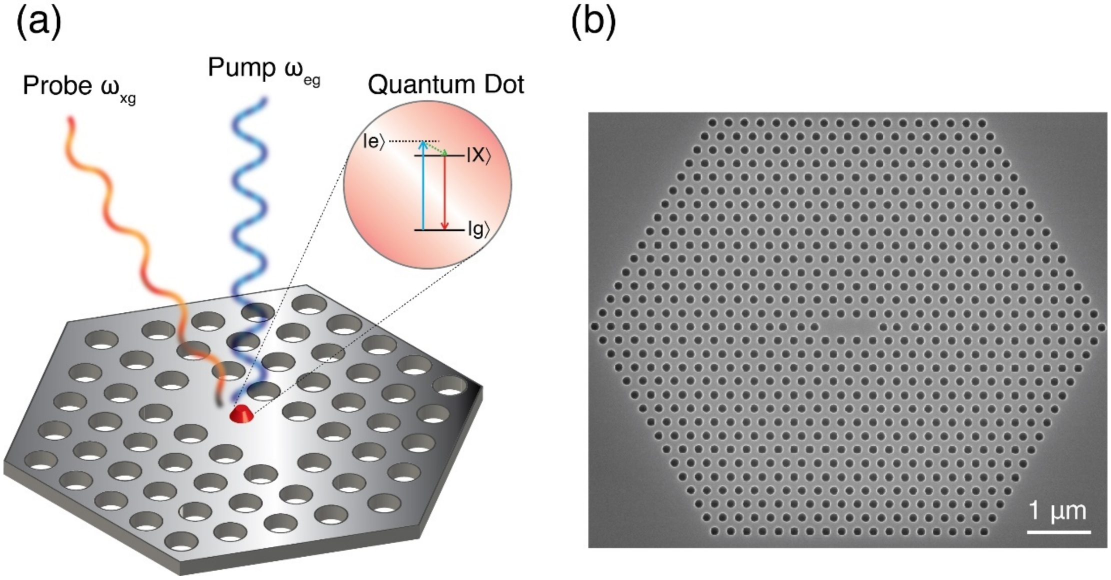

Figure 41. (a) Schematic of the measurement scheme. A quantum dot is located at the center of a photonic crystal cavity. A pump laser excites the quantum dot from its ground state to the excited state and it rapidly decays to the exciton state $|X\rangle$, while a probe laser is measuring the cavity reflectivity around the $|X\rangle \rightarrow |g\rangle$ transition. (b) SEM image of the fabricated photonic crystal cavity in GaAs.

6.3 Device characterization

Using a modified version of the setup described in 1.8, we measure the reflectivity of the cavity at different sample voltages. Unlike photoluminescence measurements in the previous chapters, reflectivity measurement requires a cross-polarization setup where the excitation and the collection have orthogonal polarizations which we achieve with two separate linear polarizers. Moreover, since the emission wavelength of InAs/GaAs quantum dots are around 930 nm, we use different sets of spectrometers and single-photon detectors.

Figure 42a represents the cavity reflectivity of the fabricated device for different sample voltages. At voltages around $620\ mV$, the quantum dot is activated and turns the spectrum into a polaritonic feature, while the spectrum remains a simple Lorentzian peak (due to the cavity) at voltages far from this value which indicates the absence of the quantum dot. In this measurement, we weakly probe the cavity reflectively, while there is a small pumping laser. Figure 42b shows the pump power dependence of emission intensity in the absence of the probe laser. We observe that the emission intensity saturates at pump powers of the order of few tens of microwatts. We use this saturation curve as a measure of the population of the $|X\rangle$ state.

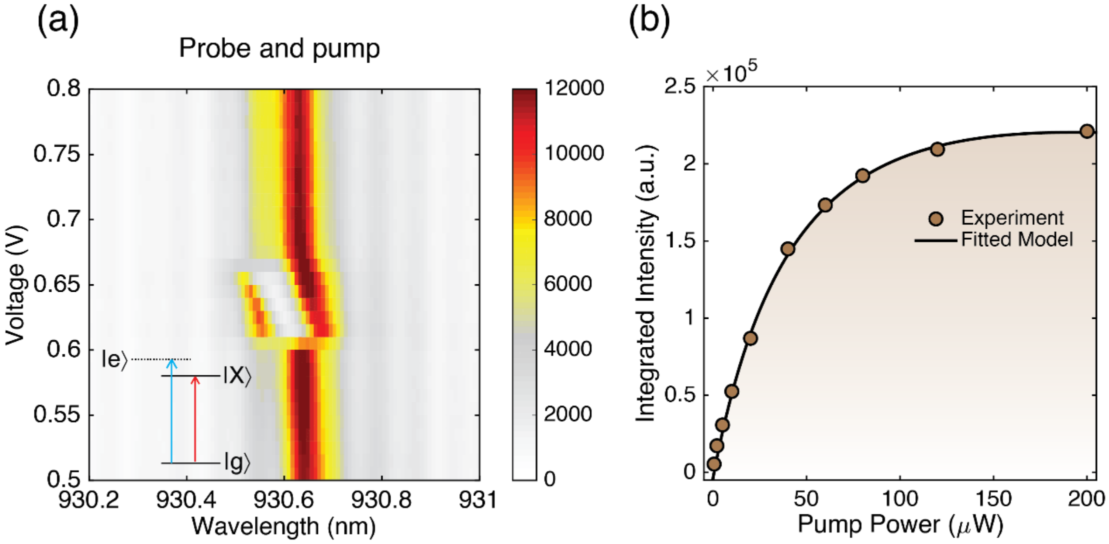

Figure 42. (a) Reflectivity of the quantum dot coupled cavity at different voltages measured at the presence of both pump and the probe. The pump-induced fluorescence is subtracted from the spectra. (b) Integrated emission intensity of the system at 620 mV for different pump powers in the absence of the probe laser.

6.4 Optical amplification

Probe signal is measured by subtracting the pump-induced fluorescence from the probe reflectivity. We further normalize this signal by the probe signal at the absence of the quantum dot. This is possible because of the electrical control on the state of the quantum dot. Figure 43a shows the normalized reflectivity of the cavity for different pump powers. At low pump powers, we observe that the reflectivity signal is attenuated at the cavity center. By increasing the pump power this attenuation decreases and eventually becomes an amplification. Figure 43b shows the measured amplification or attenuation at the cavity center compared to the case where the probe laser is far detuned from the cavity. We define this property as optical gain in the system. Optical gain goes from negative values at low pump powers to zero and positive values at larger pump powers where the quantum dot population becomes 50% or more. We attribute this amplification or gain to stimulated emission from the quantum dot when the population of $|X\rangle$ is greater than the population of ground state $|g\rangle$ (i.e., population inversion). At $80\ \mu W$ of pump power, we observe $\sim 16\%$ of optical gain which is a factor of 8 greater than the previous demonstration of optical amplification using a quantum emitter weakly coupled to a fiber-based cavity [112].

6.5 Summary and discussions

In this chapter, we have demonstrated that a cavity strongly coupled to a quantum emitter significantly enhances the optical amplification compared to the quantum emitter alone or weakly coupled cavities. This result could be of great interest both for fundamental understanding of cavity quantum electrodynamics (cQED) in solid-state systems and technological applications in low-energy optical switches and amplifiers. To further increase this optical amplification higher quality factor cavities could be implemented in fiber-based systems in which the coupling is pushed farther to the strong coupling regime [113].

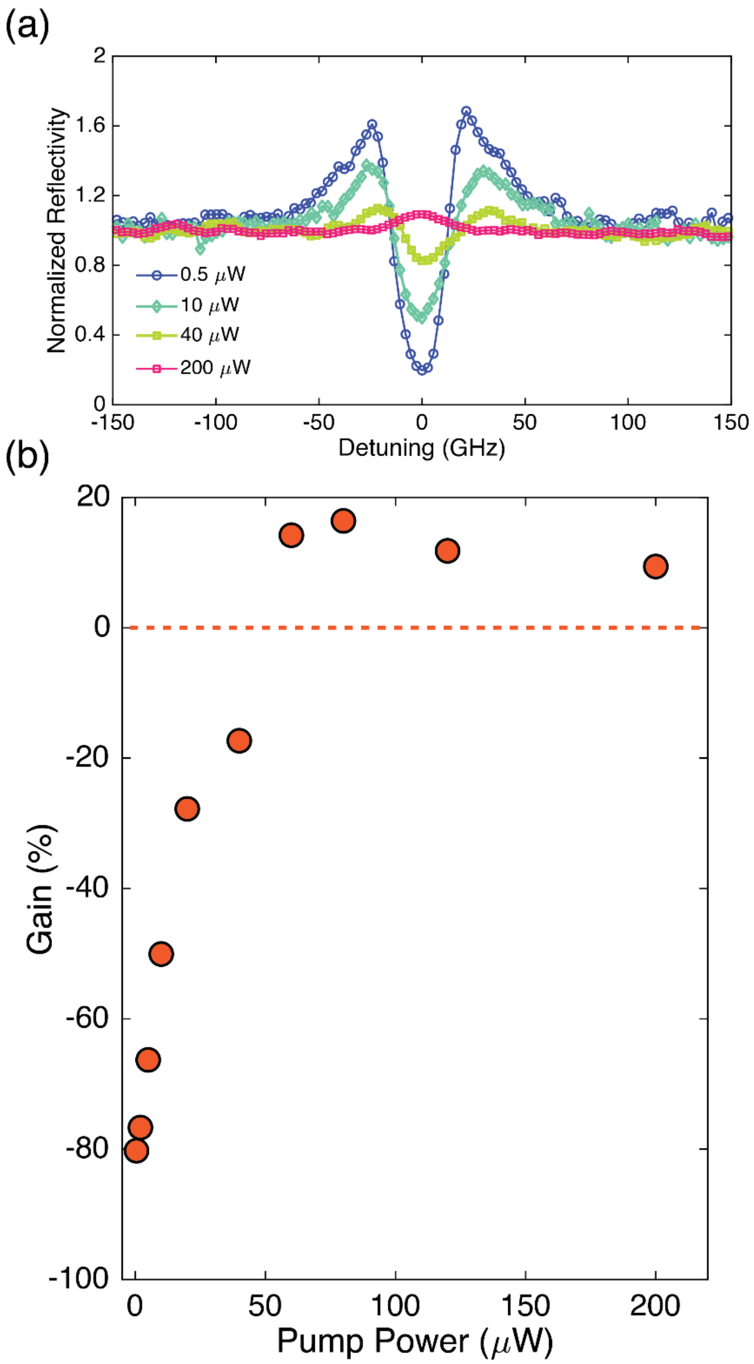

Figure 43. (a) Normalized reflectivity of the cavity at different pump powers. (b) Measured gain as a function of pump power.

Chapter 7: Conclusions and future directions

In this thesis, we have demonstrated several essential elements of an integrated quantum photonic processor. We implemented a hybrid integration approach with ultra-high precision accuracy for transferring nanostructures from one chip to another. Using this technique, we successfully transferred nanostructures containing quantum dots, efficient single-photon sources, to scalable integrated photonic platforms including silicon-on-insulator and lithium niobate. In these experiments, we confirmed single photon nature of the light with photon statistics measurements. We demonstrated on-chip filtering and routing of quantum dot emission using a silicon photonic add-drop filter. The next step in this direction would be implementing fast switches using silicon or lithium niobate photonics in order to produce time-demultiplexed single-photon sources [65].

We used quantum confined Stark effect in a electrostatic capacitor device to tune the emission energy of InAs/InP quantum dots. The tuning range provided by our approach significantly increases the potential of this material for on-chip implementation of quantum interference. Recently, strain tuning of quantum dots hosted in GaAs has enabled wavelength tuning over the entire inhomogeneous broadening and interference between three quantum dots has been demonstrated [114]. Extension of this technique to InAs/InP quantum dots could be a promising path forward for quantum communication devices operating at the telecommunication wavelengths.

In the last chapter, we discussed our preliminary results on optical gain from a single quantum dot strongly coupled to a nanophotonic cavity. Since the quantum dots are randomly placed on the sample and have different emission wavelengths, in order to have a cavity strongly coupled to a dot we had to fabricate hundreds of devices. There are several methods to improve this low device yield. Deterministic positioning of the quantum dots during the growth [115], in-situ imaging of the quantum dots during the electron beam lithography [116], cavity and quantum dot tuning techniques [117] could all be used to increase the device yield in strongly coupled systems. Moreover, to integrate with other photonic modules, strongly coupled devices need to be realized in planar geometries. This could be achieved by integration of cavities evanescently coupled to planar waveguides [53].

Ultimately, a quantum photonic circuit that is capable of performing useful information processing tasks requires all of modules described in this thesis. We are at a stage which all of the individual elements have been realized. An important task would be to connect all these individual devices in a large platform and overcome the system-level challenges that rise from wavelength and material compatibility, energy consumption, and manufacturability.

Bibliography

1. T. D. Ladd, F. Jelezko, R. Laflamme, Y. Nakamura, C. Monroe, and J. L. O'Brien, "Quantum computers," Nature **464**(7285), 45–53 (2010).
2. H. J. Kimble, "The quantum internet," Nature **453**(7198), 1023–1030 (2008).
3. P. Senellart, G. Solomon, and A. White, "High-performance semiconductor quantum-dot single-photon sources," Nat. Nanotechnol. **12**(11), 1026–1039 (2017).
4. I. Aharonovich, D. Englund, and M. Toth, "Solid-state single-photon emitters," Nat. Photonics **10**(10), 631–641 (2016).
5. F. Kaneda and P. G. Kwiat, "High-efficiency single-photon generation via large-scale active time multiplexing," Sci. Adv. **5**(10), eaaw8586 (2019).
6. P. Kolchin, N. Pholchai, M. H. Mikkelsen, J. Oh, S. Ota, M. S. Islam, X. Yin, and X. Zhang, "High Purcell Factor Due To Coupling of a Single Emitter to a Dielectric Slot Waveguide," Nano Lett. **15**(1), 464–468 (2015).
7. C. Santori, M. Pelton, G. Solomon, Y. Dale, and Y. Yamamoto, "Triggered Single Photons from a Quantum Dot," Phys. Rev. Lett. **86**(8), 1502–1505 (2001).
8. J. Wang, Y. Zhou, Z. Wang, A. Rasmita, J. Yang, X. Li, H. J. von Bardeleben, and W. Gao, "Bright room temperature single photon source at telecom range in cubic silicon carbide," Nat. Commun. **9**(1), 4106 (2018).
9. T. T. Tran, K. Bray, M. J. Ford, M. Toth, and I. Aharonovich, "Quantum emission from hexagonal boron nitride monolayers," Nat. Nanotechnol. **11**, 37 (2015).

10. T. Cai, J.-H. Kim, Z. Yang, S. Dutta, S. Aghaeimeibodi, and E. Waks, "Radiative Enhancement of Single Quantum Emitters in WSe2 Monolayers Using Site-Controlled Metallic Nanopillars," ACS Photonics **5**(9), 3466–3471 (2018).

11. J.-H. Kim, T. Cai, C. J. K. Richardson, R. P. Leavitt, and E. Waks, "Two-photon interference from a bright single-photon source at telecom wavelengths," Optica **3**(6), 577 (2016).

12. A. Biberman, M. J. Shaw, E. Timurdogan, J. B. Wright, and M. R. Watts, "Ultralow-loss silicon ring resonators," Opt. Lett. **37**(20), 4236–4238 (2012).

13. A. Rao and S. Fathpour, "Compact lithium niobate electrooptic modulators," IEEE J. Sel. Top. Quantum Electron. **24**(4), 1–14 (2018).

14. F. Marsili, V. B. Verma, J. A. Stern, S. Harrington, A. E. Lita, T. Gerrits, I. Vayshenker, B. Baek, M. D. Shaw, R. P. Mirin, and S. W. Nam, "Detecting single infrared photons with 93% system efficiency," Nat. Photonics **7**, 210 (2013).

15. F. Najafi, J. Mower, N. C. Harris, F. Bellei, A. Dane, C. Lee, X. Hu, P. Kharel, F. Marsili, S. Assefa, K. K. Berggren, and D. Englund, "On-chip detection of non-classical light by scalable integration of single-photon detectors," Nat. Commun. **6**(1), 5873 (2015).

16. Y. Chen, A. Ryou, M. R. Friedfeld, T. Fryett, J. Whitehead, B. M. Cossairt, and A. Majumdar, "Deterministic Positioning of Colloidal Quantum Dots on Silicon Nitride Nanobeam Cavities," Nano Lett. **18**(10), 6404–6410 (2018).

17. K. Tanabe, K. Watanabe, and Y. Arakawa, "III-V/Si hybrid photonic devices

by direct fusion bonding," Sci. Rep. **2**, 349 (2012).

18. R. Katsumi, Y. Ota, M. Kakuda, S. Iwamoto, and Y. Arakawa, "Transfer-printed single photon sources coupled to wire waveguides," **5**(6), 691–694 (2018).
19. I. E. Zadeh, A. W. Elshaari, K. D. Jöns, A. Fognini, D. Dalacu, P. J. Poole, M. E. Reimer, and V. Zwiller, "Deterministic Integration of Single Photon Sources in Silicon Based Photonic Circuits," Nano Lett. **16**(4), 2289–2294 (2016).
20. J. H. Kim, S. Aghaeimeibodi, C. J. K. Richardson, R. P. Leavitt, D. Englund, and E. Waks, "Hybrid Integration of Solid-State Quantum Emitters on a Silicon Photonic Chip," Nano Lett. **17**(12), 7394–7400 (2017).
21. J.-H. Kim, S. Aghaeimeibodi, J. Carolan, D. Englund, and E. Waks, "Hybrid integration methods for on-chip quantum photonics," arXiv Prepr. arXiv1911.12756 (2019).
22. S. Aghaeimeibodi, J.-H. Kim, C.-M. Lee, M. A. Buyukkaya, C. Richardson, and E. Waks, "Silicon photonic add-drop filter for quantum emitters," Opt. Express **27**(12), 16882–16889 (2019).
23. S. Aghaeimeibodi, B. Desiatov, J.-H. Kim, C.-M. Lee, M. A. Buyukkaya, A. Karasahin, C. J. K. Richardson, R. P. Leavitt, M. Lončar, and E. Waks, "Integration of Quantum Emitters with Lithium Niobate Photonics," Appl. Phys. Lett. **113**, 221102 (2018).
24. S. Aghaeimeibodi, C.-M. Lee, M. A. Buyukkaya, C. J. K. Richardson, and E. Waks, "Large stark tuning of InAs/InP quantum dots," Appl. Phys. Lett. **114**(7), 71105 (2019).

25. J. W. Silverstone, D. Bonneau, J. L. O'Brien, and M. G. Thompson, "Silicon Quantum Photonics," IEEE J. Sel. Top. Quantum Electron. **22**(6), 390–402 (2016).

26. N. C. Harris, B. Darius, P. Mihir, S. G. R, M. Jacob, P. Mihika, B.-J. Tom, H. Michael, and E. Dirk, "Large-scale quantum photonic circuits in silicon," Nanophotonics **5**, 456 (2016).

27. A. H. Atabaki, S. Moazeni, F. Pavanello, H. Gevorgyan, J. Notaros, L. Alloatti, M. T. Wade, C. Sun, S. A. Kruger, H. Meng, K. Al Qubaisi, I. Wang, B. Zhang, A. Khilo, C. V Baiocco, M. A. Popović, V. M. Stojanović, and R. J. Ram, "Integrating photonics with silicon nanoelectronics for the next generation of systems on a chip," Nature **556**(7701), 349–354 (2018).

28. J. Sun, E. Timurdogan, A. Yaacobi, E. S. Hosseini, and M. R. Watts, "Large-scale nanophotonic phased array," Nature **493**, 195 (2013).

29. N. C. Harris, D. Grassani, A. Simbula, M. Pant, M. Galli, T. Baehr-Jones, M. Hochberg, D. Englund, D. Bajoni, and C. Galland, "Integrated Source of Spectrally Filtered Correlated Photons for Large-Scale Quantum Photonic Systems," Phys. Rev. X **4**(4), 41047 (2014).

30. T. Miyazawa, K. Takemoto, Y. Nambu, S. Miki, T. Yamashita, H. Terai, M. Fujiwara, M. Sasaki, Y. Sakuma, M. Takatsu, T. Yamamoto, and Y. Arakawa, "Single-photon emission at 1.5 μ m from an InAs/InP quantum dot with highly suppressed multi-photon emission probabilities," Appl. Phys. Lett. **109**(13), 132106 (2016).

31. K. Takemoto, M. Takatsu, S. Hirose, N. Yokoyama, Y. Sakuma, T. Usuki, T.

Miyazawa, and Y. Arakawa, "An optical horn structure for single-photon source using quantum dots at telecommunication wavelength," J. Appl. Phys. **101**(8), 81720 (2007).

32. X. Ding, Y. He, Z.-C. Duan, N. Gregersen, M.-C. Chen, S. Unsleber, S. Maier, C. Schneider, M. Kamp, S. Höfling, C.-Y. Lu, and J.-W. Pan, "On-Demand Single Photons with High Extraction Efficiency and Near-Unity Indistinguishability from a Resonantly Driven Quantum Dot in a Micropillar," Phys. Rev. Lett. **116**(2), 20401 (2016).

33. Y.-M. He, Y. He, Y.-J. Wei, D. Wu, M. Atatüre, C. Schneider, S. Höfling, M. Kamp, C.-Y. Lu, and J.-W. Pan, "On-demand semiconductor single-photon source with near-unity indistinguishability," Nat. Nanotechnol. **8**, 213 (2013).

34. N. Somaschi, V. Giesz, L. De Santis, J. C. Loredo, M. P. Almeida, G. Hornecker, S. L. Portalupi, T. Grange, C. Antón, J. Demory, C. Gómez, I. Sagnes, N. D. Lanzillotti-Kimura, A. Lemaítre, A. Auffeves, A. G. White, L. Lanco, and P. Senellart, "Near-optimal single-photon sources in the solid state," Nat. Photonics **10**(5), 340–345 (2016).

35. A. Thoma, P. Schnauber, M. Gschrey, M. Seifried, J. Wolters, J.-H. Schulze, A. Strittmatter, S. Rodt, A. Carmele, A. Knorr, T. Heindel, and S. Reitzenstein, "Exploring Dephasing of a Solid-State Quantum Emitter via Time- and Temperature-Dependent Hong-Ou-Mandel Experiments," Phys. Rev. Lett. **116**(3), 33601 (2016).

36. J. Notaros, F. Pavanello, M. T. Wade, C. M. Gentry, A. Atabaki, L. Alloatti, R. J. Ram, and M. A. Popović, "Ultra-efficient CMOS fiber-to-chip grating

couplers," in *2016 Optical Fiber Communications Conference and Exhibition (OFC)* (2016), pp. 1–3.

37. J. Cardenas, C. B. Poitras, K. Luke, L. Luo, P. A. Morton, and M. Lipson, "High Coupling Efficiency Etched Facet Tapers in Silicon Waveguides," IEEE Photonics Technol. Lett. **26**(23), 2380–2382 (2014).

38. M. J. Burek, C. Meuwly, R. E. Evans, M. K. Bhaskar, A. Sipahigil, S. Meesala, B. Machielse, D. D. Sukachev, C. T. Nguyen, J. L. Pacheco, E. Bielejec, M. D. Lukin, and M. Lončar, "Fiber-Coupled Diamond Quantum Nanophotonic Interface," Phys. Rev. Appl. **8**(2), 24026 (2017).

39. M. Schwartz, E. Schmidt, U. Rengstl, F. Hornung, S. Hepp, S. L. Portalupi, K. Ilin, M. Jetter, M. Siegel, and P. Michler, "Fully on-chip single-photon Hanbury-Brown and Twiss experiment on a monolithic semiconductor-superconductor platform," Nano Lett. **18**(11), 6892–6897 (2018).

40. A. Mohan, M. Felici, P. Gallo, B. Dwir, A. Rudra, J. Faist, and E. Kapon, "Polarization-entangled photons produced with high-symmetry site-controlled quantum dots," Nat. Photonics **4**, 302 (2010).

41. C. Schneider, T. Heindel, A. Huggenberger, P. Weinmann, C. Kistner, M. Kamp, S. Reitzenstein, S. Höfling, and A. Forchel, "Single photon emission from a site-controlled quantum dot-micropillar cavity system," Appl. Phys. Lett. **94**(11), 111111 (2009).

42. J.-H. Kim, S. Aghaeimeibodi, C. J. K. Richardson, R. P. Leavitt, and E. Waks, "Super-radiant emission from quantum dots in a nanophotonic waveguide," Nano Lett. **18**(8), 4734–4740 (2018).

43. Y. Chen, J. Zhang, M. Zopf, K. Jung, Y. Zhang, R. Keil, F. Ding, and O. G. Schmidt, "Wavelength-tunable entangled photons from silicon-integrated III–V quantum dots," Nat. Commun. **7**(1), 10387 (2016).

44. A. J. Bennett, R. B. Patel, J. Skiba-Szymanska, C. A. Nicoll, I. Farrer, D. A. Ritchie, and A. J. Shields, "Giant Stark effect in the emission of single semiconductor quantum dots," Appl. Phys. Lett. **97**(3), 1–4 (2010).

45. A. Aspuru-Guzik and P. Walther, "Photonic quantum simulators," Nat. Phys. **8**(4), 285–291 (2012).

46. E. Knill, R. Laflamme, and G. J. Milburn, "A scheme for efficient quantum computation with linear optics," Nature **409**(6816), 46–52 (2001).

47. J. L. O'Brien, A. Furusawa, and J. Vučković, "Photonic quantum technologies," Nat. Photonics **3**(12), 687–695 (2009).

48. F. Böhm, N. Nikolay, C. Pyrlik, J. Schlegel, A. Thies, A. Wicht, G. Tränkle, and O. Benson, "On-Chip Integration of Single Solid-State Quantum Emitters with a SiO2 Photonic Platform," arXiv Prepr. arXiv1812.02528 (2018).

49. D. J. P. Ellis, A. J. Bennett, C. Dangel, J. P. Lee, J. P. Griffiths, T. A. Mitchell, T. K. Paraiso, P. Spencer, D. A. Ritchie, and A. J. Shields, "Independent indistinguishable quantum light sources on a reconfigurable photonic integrated circuit," Appl. Phys. Lett. **112**(21), 211104 (2018).

50. A. W. Elshaari, I. E. Zadeh, A. Fognini, M. E. Reimer, D. Dalacu, P. J. Poole, V. Zwiller, and K. D. Jöns, "On-chip single photon filtering and multiplexing in hybrid quantum photonic circuits," Nat. Commun. **8**(1), 1–8 (2017).

51. M. Davanco, J. Liu, L. Sapienza, C.-Z. Zhang, J. V. M. Cardoso, V. Verma, R.

Mirin, S. W. Nam, L. Liu, and K. Srinivasan, "Heterogeneous integration for on-chip quantum photonic circuits with single quantum dot devices," Nat. Commun. **8**(1), 889 (2017).

52. E. Murray, D. J. P. Ellis, T. Meany, F. F. Floether, J. P. Lee, J. P. Griffiths, G. A. C. Jones, I. Farrer, D. A. Ritchie, A. J. Bennett, and A. J. Shields, "Quantum photonics hybrid integration platform," Appl. Phys. Lett. **107**(17), (2015).
53. A. Osada, Y. Ota, R. Katsumi, M. Kakuda, S. Iwamoto, and Y. Arakawa, "Strongly Coupled Single-Quantum-Dot--Cavity System Integrated on a CMOS-Processed Silicon Photonic Chip," Phys. Rev. Appl. **11**(2), 24071 (2019).
54. R. Gourgues, I. E. Zadeh, A. W. Elshaari, G. Bulgarini, J. W. N. Los, J. Zichi, D. Dalacu, P. J. Poole, S. N. Dorenbos, and V. Zwiller, "Controlled integration of selected detectors and emitters in photonic integrated circuits," Opt. Express **27**(3), 3710–3716 (2019).
55. W. H. P. Pernice, C. Schuck, O. Minaeva, M. Li, G. N. Goltsman, A. V Sergienko, and H. X. Tang, "High-speed and high-efficiency travelling wave single-photon detectors embedded in nanophotonic circuits," Nat. Commun. **3**, 1325 (2012).
56. L. Midolo, S. L. Hansen, W. Zhang, C. Papon, R. Schott, A. Ludwig, A. D. Wieck, P. Lodahl, and S. Stobbe, "Electro-optic routing of photons from a single quantum dot in photonic integrated circuits," Opt. Express **25**(26), 33514–33526 (2017).
57. C. Papon, X. Zhou, H. Thyrrestrup, Z. Liu, S. Stobbe, R. Schott, A. D. Wieck,

A. Ludwig, P. Lodahl, and L. Midolo, "Nanomechanical single-photon routing," Optica **6**(4), 524–530 (2019).

58. A. W. Elshaari, E. Büyüközer, I. E. Zadeh, T. Lettner, P. Zhao, E. Schöll, S. Gyger, M. E. Reimer, D. Dalacu, P. J. Poole, K. D. Jöns, and V. Zwiller, "Strain-Tunable Quantum Integrated Photonics," Nano Lett. **18**(12), 7969–7976 (2018).
59. G. T. Reed, G. Mashanovich, F. Y. Gardes, and D. J. Thomson, "Silicon optical modulators," Nat. Photonics **4**, 518 (2010).
60. M. Gehl, C. Long, D. Trotter, A. Starbuck, A. Pomerene, J. B. Wright, S. Melgaard, J. Siirola, A. L. Lentine, and C. DeRose, "Operation of high-speed silicon photonic micro-disk modulators at cryogenic temperatures," Optica **4**(3), 374 (2017).
61. E. Timurdogan, C. V Poulton, M. J. Byrd, and M. R. Watts, "Electric field-induced second-order nonlinear optical effects in silicon waveguides," Nat. Photonics **11**, 200 (2017).
62. A. Morand, Y. Zhang, B. Martin, K. P. Huy, D. Amans, P. Benech, J. Verbert, E. Hadji, and J.-M. Fédéli, "Ultra-compact microdisk resonator filters on SOI substrate," Opt. Express **14**(26), 12814–12821 (2006).
63. R. P. Leavitt and C. J. K. Richardson, "Pathway to achieving circular InAs quantum dots directly on (100) InP and to tuning their emission wavelengths toward 1.55 µm," J. Vac. Sci. Technol. B **33**(5), 51202 (2015).
64. B. J. Frey, D. B. Leviton, and T. J. Madison, "Temperature-dependent refractive index of silicon and germanium," in *Optomechanical Technologies*

for Astronomy (2006), **6273**, p. 62732J.

65. F. Lenzini, B. Haylock, J. C. Loredo, R. A. Abrahão, N. A. Zakaria, S. Kasture, I. Sagnes, A. Lemaitre, H.-P. Phan, D. V. Dao, P. Senellart, M. P. Almeida, A. G. White, and M. Lobino, "Active demultiplexing of single photons from a solid-state source," Laser Photon. Rev. **11**(3), 1600297 (2017).
66. J. Carolan, C. Harrold, C. Sparrow, E. Martín-López, N. J. Russell, J. W. Silverstone, P. J. Shadbolt, N. Matsuda, M. Oguma, M. Itoh, G. D. Marshall, M. G. Thompson, J. C. F. Matthews, T. Hashimoto, J. L. O'Brien, and A. Laing, "Universal linear optics.," Science **349**(6249), 711–6 (2015).
67. H. Wang, Y. He, Y.-H. Li, Z.-E. Su, B. Li, H.-L. Huang, X. Ding, M.-C. Chen, C. Liu, J. Qin, and others, "High-efficiency multiphoton boson sampling," Nat. Photonics **11**(6), 361 (2017).
68. G. Poberaj, H. Hu, W. Sohler, and P. Guenter, "Lithium niobate on insulator (LNOI) for micro-photonic devices," Laser Photon. Rev. **6**(4), 488–503 (2012).
69. A. Guarino, G. Poberaj, D. Rezzonico, R. Degl'Innocenti, and P. Günter, "Electro–optically tunable microring resonators in lithium niobate," Nat. Photonics **1**, 407 (2007).
70. R. Weis and T. Gaylord, "Lithium Niobate: Summary of Physical Properties and Crystal Structure R.," Appl. Phys. A Mater. Sci. Process. **37**(4), 191–203 (1985).
71. E. L. Wooten, K. M. Kissa, A. Yi-Yan, E. J. Murphy, D. a. Lafaw, P. F. Hallemeier, D. Maack, D. V. Attanasio, D. J. Fritz, G. J. McBrien, and D. E. Bossi, "A review of lithium niobate modulators for fiber-optic communications

systems," IEEE J. Sel. Top. Quantum Electron. **6**(1), 69–82 (2000).

72. D. N. Nikogosyan, *Nonlinear Optical Crystals: A Complete Survey* (Springer Science & Business Media, 2006).

73. R. V. Schmidt and I. P. Kaminow, "Metal-diffused optical waveguides in LiNbO3," Appl. Phys. Lett. **25**(8), 458–460 (1974).

74. M. Zhang, C. Wang, R. Cheng, A. Shams-Ansari, and M. Loncar, "Monolithic Ultrahigh-Q Lithium Niobate Microring Resonator," Optica **4**(12), 1536–1537 (2017).

75. I. Krasnokutska, J.-L. J. Tambasco, X. Li, and A. Peruzzo, "Ultra-low loss photonic circuits in Lithium Niobate On Insulator," Opt. Express **26**(2), (2018).

76. M. R. Escalé, D. Pohl, A. Sergeyev, and R. Grange, "Extreme electro-optic tuning of Bragg mirrors integrated in lithium niobate nanowaveguides," Opt. Lett. **43**(7), 1515–1518 (2018).

77. G. Ulliac, V. Calero, A. Ndao, F. I. Baida, and M.-P. Bernal, "Argon plasma inductively coupled plasma reactive ion etching study for smooth sidewall thin film lithium niobate waveguide application," Opt. Mater. (Amst). **53**, 1–5 (2016).

78. C. Wang, M. Zhang, B. Stern, M. Lipson, and M. Loncar, "Nanophotonic Lithium Niobate Electro-optic Modulators," Opt. Express **26**(2), 1547–1555 (2018).

79. A. Politi, J. C. F. Matthews, and J. L. O'Brien, "Shor's quantum factoring algorithm on a photonic chip," Science **325**(5945), 1221 (2009).

80. P. Kok, W. J. Munro, K. Nemoto, T. C. Ralph, J. P. Dowling, and G. J.

Milburn, "Linear optical quantum computing with photonic qubits," Rev. Mod. Phys. **79**(1), 135–174 (2007).

81. X. Qiang, X. Zhou, J. Wang, C. M. Wilkes, T. Loke, S. O'Gara, L. Kling, G. D. Marshall, R. Santagati, T. C. Ralph, J. B. Wang, J. L. O'Brien, M. G. Thompson, and J. C. F. Matthews, "Large-scale silicon quantum photonics implementing arbitrary two-qubit processing," Nat. Photonics **12**, 534 (2018).
82. A. Peruzzo, M. Lobino, J. C. F. Matthews, N. Matsuda, A. Politi, K. Poulios, X.-Q. Zhou, Y. Lahini, N. Ismail, K. Wörhoff, Y. Bromberg, Y. Silberberg, M. G. Thompson, and J. L. O'Brien, "Quantum walks of correlated particles," Science **329**(5998), 1500–1504 (2010).
83. G. Panitchayangkoon, D. Hayes, K. A. Fransted, J. R. Caram, E. Harel, J. Wen, R. E. Blankenship, and G. S. Engel, "Long-lived quantum coherence in photosynthetic complexes at physiological temperature," Proc. Natl. Acad. Sci. **107**(29), 12766–12770 (2010).
84. A. Faraon, I. Fushman, D. Englund, N. Stoltz, P. Petroff, and J. Vučković, "Coherent generation of non-classical light on a chip via photon-induced tunnelling and blockade," Nat. Phys. **4**, 859 (2008).
85. S. Sun, H. Kim, Z. Luo, G. S. Solomon, and E. Waks, "A single-photon switch and transistor enabled by a solid-state quantum memory," Science **361**(6397), 57–60 (2018).
86. R. Bäumner, L. Bonacina, J. Enderlein, J. Extermann, T. Fricke-Begemann, G. Marowsky, and J.-P. Wolf, "Evanescent-field-induced second harmonic generation by noncentrosymmetric nanoparticles," Opt. Express **18**(22),

23218–23225 (2010).

87. B. Desiatov, A. Shams-Ansari, M. Zhang, C. Wang, and M. Lončar, "Ultra-low-loss integrated visible photonics using thin-film lithium niobate," Optica **6**(3), 380–384 (2019).

88. X. Ding, Y. He, Z. C. Duan, N. Gregersen, M. C. Chen, S. Unsleber, S. Maier, C. Schneider, M. Kamp, S. Höfling, C. Y. Lu, and J. W. Pan, "On-Demand Single Photons with High Extraction Efficiency and Near-Unity Indistinguishability from a Resonantly Driven Quantum Dot in a Micropillar," Phys. Rev. Lett. **116**(2), 1–6 (2016).

89. K. H. Madsen, S. Ates, J. Liu, A. Javadi, S. M. Albrecht, I. Yeo, S. Stobbe, and P. Lodahl, "Efficient out-coupling of high-purity single photons from a coherent quantum dot in a photonic-crystal cavity," Phys. Rev. B **90**(15), 155303 (2014).

90. M. Schwartz, E. Schmidt, U. Rengstl, F. Hornung, S. Hepp, S. L. Portalupi, K. Ilin, M. Jetter, M. Siegel, and P. Michler, "Fully on-chip single-photon Hanbury-Brown and Twiss experiment on a monolithic semiconductor-superconductor platform," arXiv Prepr. arXiv1806.04099 (2018).

91. K. Mnaymneh, D. Dalacu, J. McKee, J. Lapointe, S. Haffouz, J. F. Weber, D. B. Northeast, P. J. Poole, G. C. Aers, and R. L. Williams, "On-Chip Integration of Single Photon Sources via Evanescent Coupling of Tapered Nanowires to SiN Waveguides," Adv. Quantum Technol. **n/a**(n/a), 1900021 (2019).

92. T. Miyazawa, K. Takemoto, Y. Sakuma, S. Hirose, T. Usuki, N. Yokoyama, M. Takatsu, and Y. Arakawa, "Single-photon generation in the 1.55-μm

optical-fiber band from an InAs/InP quantum dot," Jpn. J. Appl. Phys. **44**(5L), L620 (2005).

93. M. D. Birowosuto, H. Sumikura, S. Matsuo, H. Taniyama, P. J. Van Veldhoven, R. Nötzel, and M. Notomi, "Fast Purcell-enhanced single photon source in 1,550-nm telecom band from a resonant quantum dot-cavity coupling," Sci. Rep. **2**, 321 (2012).

94. S. Ramanathan, G. Petersen, K. Wijesundara, R. Thota, E. A. Stinaff, M. L. Kerfoot, M. Scheibner, A. S. Bracker, and D. Gammon, "Quantum-confined Stark effects in coupled InAs/GaAs quantum dots," Appl. Phys. Lett. **102**(21), 213101 (2013).

95. A. J. Bennett, R. B. Patel, J. Skiba-Szymanska, C. A. Nicoll, I. Farrer, D. A. Ritchie, and A. J. Shields, "Giant Stark effect in the emission of single semiconductor quantum dots," Appl. Phys. Lett. **97**(3), 31104 (2010).

96. R. B. Patel, A. J. Bennett, I. Farrer, C. A. Nicoll, D. A. Ritchie, and A. J. Shields, "Two-photon interference of the emission from electrically tunable remote quantum dots," Nat. Photonics **4**(9), 632 (2010).

97. M. Petruzzella, T. Xia, F. Pagliano, S. Birindelli, L. Midolo, Z. Zobenica, L. H. Li, E. H. Linfield, and A. Fiore, "Fully tuneable, Purcell-enhanced solid-state quantum emitters," Appl. Phys. Lett. **107**(14), 141109 (2015).

98. S. Gordon, M. Yacob, J. P. Reithmaier, M. Benyoucef, and A. Zrenner, "Coherent photocurrent spectroscopy of single InP-based quantum dots in the telecom band at 1.5 µm," Appl. Phys. B **122**(2), 37 (2016).

99. M. E. Reimer, D. Dalacu, J. Lapointe, P. J. Poole, D. Kim, G. C. Aers, W. R.

McKinnon, and R. L. Williams, "Single electron charging in deterministically positioned InAs/InP quantum dots," Appl. Phys. Lett. **94**(1), 11108 (2009).

100. M. E. Reimer, D. Dalacu, J. Lapointe, P. J. Poole, W. R. McKinnon, and R. L. Williams, "Non-inverted electron--hole alignment in InAs/InP self-assembled quantum dots," Phys. status solidi **246**(4), 828–831 (2009).

101. T. B. Hoang, J. Beetz, M. Lermer, L. Midolo, M. Kamp, S. Höfling, and A. Fiore, "Widely tunable, efficient on-chip single photon sources at telecommunication wavelengths," Opt. Express **20**(19), 21758–21765 (2012).

102. P. W. Fry, J. J. Finley, L. R. Wilson, A. Lemaitre, D. J. Mowbray, M. S. Skolnick, M. Hopkinson, G. Hill, and J. C. Clark, "Electric-field-dependent carrier capture and escape in self-assembled InAs/GaAs quantum dots," Appl. Phys. Lett. **77**(26), 4344–4346 (2000).

103. R. Oulton, J. J. Finley, A. D. Ashmore, I. S. Gregory, D. J. Mowbray, M. S. Skolnick, M. J. Steer, S.-L. Liew, M. A. Migliorato, and A. J. Cullis, "Manipulation of the homogeneous linewidth of an individual In (Ga) As quantum dot," Phys. Rev. B **66**(4), 45313 (2002).

104. J.-H. Kim, C. J. K. Richardson, R. P. Leavitt, and E. Waks, "Two-photon interference from the far-field emission of chip-integrated cavity-coupled emitters," Nano Lett. **16**(11), 7061–7066 (2016).

105. B. Alén, J. Bosch, D. Granados, J. Martínez-Pastor, J. M. García, and L. González, "Oscillator strength reduction induced by external electric fields in self-assembled quantum dots and rings," Phys. Rev. B **75**(4), 45319 (2007).

106. L. Kinnischtzke, K. M. Goodfellow, C. Chakraborty, Y.-M. Lai, S. Fält, W.

Wegscheider, A. Badolato, and A. N. Vamivakas, "Graphene mediated Stark shifting of quantum dot energy levels," Appl. Phys. Lett. **108**(21), 211905 (2016).

107. A. D. Mohite, P. Gopinath, H. M. Shah, and B. W. Alphenaar, "Exciton dissociation and stark effect in the carbon nanotube photocurrent spectrum," Nano Lett. **8**(1), 142–146 (2008).

108. P. Lodahl, S. Mahmoodian, and S. Stobbe, "Interfacing single photons and single quantum dots with photonic nanostructures," Rev. Mod. Phys. **87**(2), 347 (2015).

109. Z. Luo, S. Sun, A. Karasahin, A. S. Bracker, S. G. Carter, M. K. Yakes, D. Gammon, and E. Waks, "A Spin–Photon Interface Using Charge-Tunable Quantum Dots Strongly Coupled to a Cavity," Nano Lett. **19**(10), 7072–7077 (2019).

110. J. Hwang, M. Pototschnig, R. Lettow, G. Zumofen, A. Renn, S. Götzinger, and V. Sandoghdar, "A single-molecule optical transistor," Nature **460**(7251), 76–80 (2009).

111. Y. Akahane, T. Asano, B.-S. Song, and S. Noda, "High-Q photonic nanocavity in a two-dimensional photonic crystal," Nature **425**(6961), 944–947 (2003).

112. D. Wang, H. Kelkar, D. Martin-Cano, T. Utikal, S. Götzinger, and V. Sandoghdar, "Coherent Coupling of a Single Molecule to a Scanning Fabry-Perot Microcavity," Phys. Rev. X **7**(2), 21014 (2017).

113. D. Najer, I. Söllner, P. Sekatski, V. Dolique, M. C. Löbl, D. Riedel, R. Schott, S. Starosielec, S. R. Valentin, A. D. Wieck, N. Sangouard, A. Ludwig, and R.

J. Warburton, "A gated quantum dot strongly coupled to an optical microcavity," Nature (2019).

114. J. Q. Grim, A. S. Bracker, M. Zalalutdinov, S. G. Carter, A. C. Kozen, M. Kim, C. S. Kim, J. T. Mlack, M. Yakes, B. Lee, and D. Gammon, "Scalable in operando strain tuning in nanophotonic waveguides enabling three-quantum-dot superradiance," Nat. Mater. **18**(9), 963–969 (2019).

115. C. Schneider, M. Strauß, T. Sünner, A. Huggenberger, D. Wiener, S. Reitzenstein, M. Kamp, S. Höfling, and A. Forchel, "Lithographic alignment to site-controlled quantum dots for device integration," Appl. Phys. Lett. **92**(18), 183101 (2008).

116. P. Schnauber, J. Schall, S. Bounouar, T. Höhne, S.-I. Park, G.-H. Ryu, T. Heindel, S. Burger, J.-D. Song, S. Rodt, and S. Reitzenstein, "Deterministic Integration of Quantum Dots into on-Chip Multimode Interference Beamsplitters Using in Situ Electron Beam Lithography," Nano Lett. **18**(4), 2336–2342 (2018).

117. J. L. Zhang, S. Sun, M. J. Burek, C. Dory, Y.-K. Tzeng, K. A. Fischer, Y. Kelaita, K. G. Lagoudakis, M. Radulaski, Z.-X. Shen, N. A. Melosh, S. Chu, M. Lončar, and J. Vučković, "Strongly Cavity-Enhanced Spontaneous Emission from Silicon-Vacancy Centers in Diamond," Nano Lett. **18**(2), 1360–1365 (2018).